Ocean Sci. Discuss., 11, 1023–1091, 2014
www.ocean-sci-discuss.net/11/1023/2014/
doi:10.5194/osd-11-1023-2014


Ocean Science Discussions
Open Access



# Assessment of the ECCO2 reanalysis on the representation of Antarctic Bottom Water properties

**M. Azaneu, R. Kerr, and M. M. Mata**

Laboratório de Estudos dos Oceanos e Clima, Instituto de Oceanografia, Universidade Federal do Rio Grande (FURG), Rio Grande, RS, 96203-900, Brazil

Received: 19 February 2014 – Accepted: 14 March 2014 – Published: 28 March 2014

Correspondence to: M. Azaneu (m.azaneu@furg.br)

Published by Copernicus Publications on behalf of the European Geosciences Union.







## Abstract

We analyzed the ability of the Estimating the Circulation and Climate of the Ocean – Phase II (ECCO2) reanalysis to represent the hydrographic properties and variability of the Antarctic Bottom Water (AABW) in the Southern Ocean. We used a twenty-year observational database to perform comparisons of hydrographic properties and reanalysis data for the same time period (1992–2011). In addition, we evaluated four *case studies* based on current meter data and the AABW volume transport estimates previously reported in the literature. The main Southern Ocean oceanographic features, as well as the characteristic shape of the regional potential temperature–salinity ($\theta$–$S$) diagrams, are adequately represented by the reanalysis. However, the opening of an oceanic polynya in the Weddell Sea Sector, which has been clearly visible since 2005, contributed to an unrealistic representation of the hydrographic properties of the Southern Ocean primarily after 2004. In this sense, our analyses focused on the period that was identified as more reliable (1992–2004). In general, the reanalysis data showed surface waters that were warmer, saltier, and denser than observations, which may have resulted from the absence of Ice Shelf Water and from the overestimation of sea ice concentrations that limit oceanic heat loss during austral winters. Intermediate waters were generally colder, fresher, and denser than observations, whereas deep waters were warmer and less dense. These differences in deep water properties were partially a result of the inability to reproduce the densest AABW variety by reanalysis for most of the analyzed period and also because of the model's relatively coarse vertical resolution. Despite differences in absolute values, the upper AABW limit ($\gamma^n \geq 28.27\,\mathrm{kg\,m^{-3}}$) and AABW occupied area were well represented in the WOCE repeat sections SR2 and SR4 for the studied periods. In section WOCE SR3, however, the estimates from the differences were not as well correlated, and the AABW layer thickness was underrepresented. The *case studies* showed a good representation of the AABW volume export and current velocity variability in the most important region of dense water export (i.e., the Weddell Sea). The exception is the AABW volume





OSD
11, 1023–1091, 2014



transport near the Kerguelen Plateau, in which the rugged local bathymetry and the relatively coarse model resolution hampered a fair representation of the transport variability by the reanalysis. Despite the consistency in terms of variability, absolute volume transport, and velocity, estimates were underrepresented in all cases. Moreover, the reanalysis was capable of reproducing the general variability pattern and trends of the AABW hydrographic properties reported by previous studies. Therefore, the ECCO2 data from the 1992–2004 period was considered adequate for investigating the circulation of the AABW and variability of the hydrographic properties, whereas data from the latter period (2005–2011) must be given careful attention.

## 1 Introduction

The Antarctic Bottom Water (AABW) covers the majority of the ocean's abyssal layer and fills and ventilates the deepest basins of the global ocean. Dense bottom water formation and spread, which occur mainly as deep western boundary currents, are important physical processes that contribute to the variability of the global overturning circulation deep cell (Talley, 2013). The meridional overturning circulation cells are the main mechanisms that are responsible for the interbasin exchange of mass, heat, salt, carbon, and nutrients; therefore, they substantially contribute to global climate regulation (e.g., Rahmstorf, 2006; Lumpkin and Speer, 2007).

The AABW formation occurs regionally around the Antarctic margin through the mixing of intermediate waters with near-freezing point shelf waters (e.g., Carmack and Foster, 1975; Foldvik et al., 1985; Nicholls et al., 2009). The latter results from shelf waters that are modified by atmospheric interaction and brine rejection during sea ice production (High Salinity Shelf Water – HSSW and Low Salinity Shelf Water – LSSW) and also by cooling through basal contact with floating ice shelves (Ice Shelf Water – ISW). The saltiest AABW variety is the Ross Sea Bottom Water, which is ultimately derived from the highest salinity shelf water present over the western Ross Sea (Jacobs et al., 1970; Orsi et al., 1999). The Weddell Sea is considered the main contributor to





OSD
11, 1023–1091, 2014



the AABW formation (Rintoul, 1998; Orsi et al., 1999). The Weddell Sea Bottom Water (WSBW) is the densest local AABW variety in the Weddell Sea and is produced through a mixture of either HSSW with Warm Deep Water (WDW – a regional variety of Circumpolar Deep Water – CDW) and Winter Water (Foster and Carmack, 1976) or ISW with WDW or modified WDW (Foldvik et al., 1985). The WSBW is mostly confined to the Weddell basin (Orsi et al., 1993); however, the Weddell Sea Deep Water (WSDW) overlies it and is light enough to spread into the global ocean through the narrow passages of the South Scotia Ridge (Muench and Hellmer, 2002; Franco et al., 2007). The WSDW can be formed either directly by entrainment during the downslope flow of dense plumes from the shelf or by a mixture of the WSBW with WDW (Orsi et al., 1993; Orsi et al., 1999; Meredith et al., 2000). Eventually, bottom water formation can occur in the open ocean region through deep convection, such as occurred with the Weddell Polynya observed during the successive winters of 1974–1976 (Gordon, 1977). During this process, there is an intense heat loss to the atmosphere, which decreases vertical stability and allows open ocean deep convection to depths much deeper than usual (Killworth, 1983).

The dominant characteristics of regional AABW varieties depend on the local type of shelf water and on complex local physical processes that are coupled and related to sea ice formation, such as the opening of coastal polynyas, ice shelf basal melting, and mixing with overlying waters (Gill, 1973; Carmack and Foster, 1975; Foldvik et al., 1985; Orsi et al., 1999; Nicholls et al., 2009). Most of the Antarctic sea ice has a high seasonal cycle, and the coverage area varies up to 80 %, reaching up to 20 million $km^2$ in austral winter (e.g., Zwally et al., 1979). In the summer, freshwater from ice melt plays a key role in the modification of Antarctic Surface Waters (AASW), whereas brine rejection in winter resulting from sea ice formation enhances shelf water salinity and contributes to dense water formation.

Several studies have reported changes in the hydrographic properties of the AABW source waters during recent decades; these changes include freshening of dense waters in the Weddell and Ross Seas shelf regions (e.g., Jacobs et al., 2002; Jacobs and





OSD
11, 1023–1091, 2014



Giulivi, 2010; Jacobs, 2004; Hellmer et al., 2011; Azaneu et al., 2013). In addition, long-term warming was observed for the intermediate waters of the Antarctic Circumpolar Current (during the 1990s; Gille, 2002) and WDW within the Weddell Gyre (1970s–1990s, Robertson et al., 2002). In turn, properties of the AABW recently formed have also been changed over the years. The WSBW in the inner Weddell Sea and the Prime Meridian experienced warming during the second half of the 1990s ($0.01\,^{\circ}\mathrm{C\,yr^{-1}}$ and $0.003\,^{\circ}\mathrm{C\,yr^{-1}}$, respectively; Fahrbach et al., 2004). A more extended study reported a WSDW and WSBW temperature and salinity increase (1998–2008) after a decreasing period from 1984–1992 (Fahrbach et al., 2011). Moreover, freshening has been observed in the AABW within the Indian and Pacific sectors of the Southern Ocean (1995–2005; Rintoul, 2007). Abyssal waters in the Australian–Antarctic Basin and also at the Princess Elizabeth Trough experienced warming (0.1 °C and 0.05 °C) and freshening (−0.005 and −0.01) between 1994/1995 and 2007 (Johnson et al., 2008). The contraction of the AABW was reported by Purkey and Johnson (2010) during the 1990s–2000s. In addition to its warming and density decrease during the last fifty years (1958–2011), Azaneu et al. (2013) also found a reduction in the AABW volume. Consistent with these findings, a decrease in the WSBW contributions (∼ 20 %) to the total water mass mixture in the Weddell Basin was identified during the 1980s–1990s near the Greenwich Meridian and at the tip of the Antarctic Peninsula (Kerr et al., 2009).

Despite the possible global implications of these long-term changes, the limited and summer-biased sampling in the Southern Ocean precludes a better understanding of the connections between these processes and the embedded physical mechanisms. Ocean modeling powered by data assimilation products offers a potentially useful tool to fill the information gaps of observational data in terms of spatial and temporal resolution by providing a more synoptic and holistic view of the main processes acting on observed changes. However, the ability and consistency of these products still need to be evaluated and investigated (Dotto et al., 2014), particularly for the deep Southern Ocean, where the available in situ dataset is still sparse in both time and space (e.g., Rintoul et al., 2012).





OSD
11, 1023–1091, 2014



Our study aims to evaluate the representation of hydrographic properties and the variability of the AABW in the Southern Ocean from the *Estimating the Circulation and Climate of the Ocean – Phase II* (ECCO2) reanalysis data. Over the last decade, several global ocean data assimilation products have been developed based on the synthesis of observations through the physics described by global ocean general circulation models (Lee et al., 2010). The original ECCO project was established in 1998 as part of the *World Ocean Circulation Experiment* (WOCE), with the intent of generating a quantitative reproduction of the time-evolution of ocean states (Menemenlis et al., 2008); this project has focused on decadal and long-term climate changes (Wunsch, 2009). However, the ECCO solutions were limited by the coarse resolution and absence of sea ice representation. Thus, the ECCO2 was created to improve these deficiencies by producing a global eddy-permitting solution that includes sea ice. Moreover, the ECCO2 presents both realistic and dynamically consistent simulations because it is generated by a model that is forward run using optimized values of control parameters (Menemenlis et al., 2008). Therefore, the reanalysis product ECCO2 presents itself as a potentially valuable tool for ocean variability and long-term change studies. Therefore, the assessment of the ECCO2 reanalysis products based on their reproduction of properties and variability of such climate-impacting water masses as the AABW is fundamental for guaranteeing the future use of these data with respect to the Southern Ocean hydrography and decadal variability.

## 2 Data and methods

### 2.1 ECCO2 reanalysis product

The ECCO2 data synthesis is based on a global full-depth ocean and sea ice configuration from the Massachusetts Institute of Technology general circulation model (MITgcm; Marshall et al., 1997). The model configuration for this product has a cube-sphere grid with a mean horizontal grid spacing of 18 km and 50 vertical levels ranging from 10 m





OSD
11, 1023–1091, 2014



thick near the surface to approximately 450 m thick at the deepest level. The model resolution is eddy-permitting at higher latitudes. The ocean global circulation model is coupled to a sea ice model that computes sea ice thickness, sea ice concentration, and snow cover, which allows the system to be constrained by polar satellite observations (Zhang et al., 1998). A Green's function approach is used to adjust the control parameters by reducing the model-data misfit (Menemenlis et al., 2005). The data constraints include sea level anomalies from altimeter data; time-mean sea levels from Maximenko and Niiler (2005); sea surface temperatures from the Group for High Resolution Sea Surface Temperature (GHRSST); temperature and salinity profiles, including the *World Ocean Circulation Experiment* (WOCE), TAO, ARGO, and XBT; sea ice concentration from passive microwave data; sea ice motion from radiometers, QuikSCAT, and RADARSAT Geophysical Processing System (RGPS); and sea ice thickness from Upward Looking Sonar (ULS) (Menemenlis et al., 2008).

The ECCO2 reanalysis products have been used for several scientific applications, such as studying the effect of extreme North Atlantic Oscillation forcing the freshwater budget in the Artic (Condron et al., 2009) and formation of the upper Arctic halocline (Nguyen et al., 2009). Using a regional configuration with a high-resolution (4 km horizontal) grid, Rignot et al. (2012) examined the spreading pattern of warm subtropical-origin waters around Greenland in 1992–2009 and observed warming of subsurface waters in the subpolar gyre. In the Southern Ocean, the ECCO2 reanalysis was used to evaluate meridional heat transport mechanisms (Volkov et al., 2010). Mazloff et al. (2010) developed a preliminary solution with a 1/6° resolution for the Southern Ocean by applying an adjoint-based state estimation on a regional scale for the 2005–2010 period (Southern Ocean State Estimate – SOSE). More recently, the analysis of Lagrangian trajectories was applied to this high resolution product to show that the pathways of the different sources of AABW amalgamates into one pathway even before they reach 31° S in the deep subtropical basins (van Sebille et al., 2013).

In this work, we used the solution "*cube 92*" (version identifier) with a 0.25° regular latitude–longitude grid. The surface forcing of this solution is provided by the





OSD
11, 1023–1091, 2014



Japan Meteorological Agency and Central Research Institute of Electric Power Industry 25 year reanalysis (JRA-25; Onogi et al., 2007). The data used in this study span from 1992 to 2011 and cover the geographic area south of 60° S. The parameters evaluated were monthly fields of potential temperature ($\theta$), salinity ($S$), and the ocean current zonal ($u$) and meridional ($v$) velocity components as well as daily surface wind stress, sea ice thickness, and ice-covered area-percent data. Computed neutral density fields ($\gamma^n$; Jackett and McDougall, 1997) were used for water masses definitions.

## 2.2 Observational datasets

### 2.2.1 Hydrographic dataset used for reanalysis assessment

The observational dataset used here was compiled from datasets of the World Ocean Database 2009, 1958–2011 (WOD09, Boyer et al., 2009); the Alfred Wegener Institute, 2003–2010; and the Brazilian High Latitude Oceanography Group (GOAL; www.goal.furg.br) CTD data, 2003–2011. More details about the dataset can be found in Azaneu et al. (2013). The combined dataset covers waters south of 60° S over a 54 year period (1958–2011), as shown in Fig. 1.

The three WOCE repeated sections (SR4, SR3, and SR2; Fig. 1) were selected to evaluate the entire ECCO2 water column representation. The western part of WOCE section SR4 is located in the main outflow route of the AABW export (e.g., Naveira Garabato et al., 2002; Kerr et al., 2012), whereas the WOCE SR2/A12 (South Africa to Antarctica) section refers to the recirculation flow of the AABW within the Weddell Gyre (WG; e.g., Klatt et al., 2005). The cross-slope section of WOCE SR3 is located in the Australian-Antarctic Basin and crosses the AABW westward flow away from its main regional sources (Ross Sea, Adelie and George V Land regions; Rintoul, 1998; Shimada et al., 2012). The cross-sections WOCE SR2 and WOCE SR3 are limited to south of 60° S in this study. The data sampling sites and dates are summarized in Fig. 1. Those sections were defined because of the availability of historical data in close proximity; the historical data were used to maximize the number of observations. In





OSD
11, 1023–1091, 2014



addition, those specific occupations occurred during the time coverage of the ECCO2 simulation, providing a synoptic comparison.

The ocean current velocity data from previous studies were used for comparison in specific *case studies*. The data from moorings M2/M3 within the Weddell Sea (Fig. 1; Gordon et al., 2010) and moorings M233/M229 (Fig. 1; Klatt et al., 2005) along the Prime Meridian were compared with the ECCO2 product. Time series of the cross-section of the AABW volume transport at the northwestern Weddell Sea (from Fahrbach et al. (2001) and Kerr et al. (2012); *Section* II in Fig. 1) and east of the Kerguelen plateau (from Fukamachi et al. (2010); *Section* I in Fig. 1) were also used for comparison with the ECCO2 estimates. The case *studies* are summarized in Table 2.

### 2.2.2 Sea ice data

The monthly sea ice concentration dataset from the National Snow and Ice Data Center was based on brightness temperature measurements derived from several passive microwave instruments (Nimbus-7 Scanning Multichannel Microwave Radiometer; the Defense Meteorological Satellite Program (DMSP) F8, F11, and F13 Special Sensor Microwave/Imagers; and the DMSP-F17 Special Sensor Microwave Imager/Sounder; NSIDC; Cavalieri et al., 2006). The data were generated using the NASA Team algorithm developed by the Oceans and Ice Branch, Laboratory for Hydrospheric Processes at the NASA Goddard Space Flight Center. Sea ice concentration data refer to the percentage of pixel area (25 km × 25 km) covered by ice and spans from October 1978 to December 2010. In this work, we only used data concurrent with the ECCO2 reanalysis period (1992–2010).

A monthly time series of sea ice-covered area percentages was determined based on the average percentage of pixels over the Southern Ocean. Pixels showing less than 15 % of the covered area were not considered to be covered by ice (Cavalieri et al., 2006).





OSD
11, 1023–1091, 2014



## 2.3 AABW definition

Our assessments are focused on the representation of the AABW, defined here as Southern Ocean waters denser than $\gamma^n = 28.27\,\mathrm{kg\,m^{-3}}$. We have not considered dense shelf waters, which are limited by the 1300 m isobath. This definition based on neutral density surface includes all the several varieties of the AABW produced around the Southern Ocean continental margins (e.g., Whitworth et al., 1998) and exported to the world ocean (as described by Orsi et al., 1999). This density-based definition of the AABW was recently applied in a model-based investigation of the AABW production and export (Kerr et al., 2012) and also in an analysis of long-term AABW hydrographic property variability (Azaneu et al., 2013).

## 2.4 Methods for reanalysis and in situ data comparison

### 2.4.1 Hydrographic properties

Three depth ranges were selected for determining climatological averages. The surface (SL), intermediate (IL), and bottom (BL) layers result from the average of the ECCO2 levels from 100–150 m, 409–634 m, and 3000 m to the seabed, respectively. The observational data were also averaged into those levels, and both datasets were spatially averaged into a 1° grid to allow the determination of the differences between fields. These estimates were the only case in which the data from the entire year period were considered. Further reanalysis-observation comparisons presented here were made based only on data from the austral summer (i.e., defined here from November to March) to avoid a possible bias because of a lack of in situ observations during other seasons. The time average of in situ data was calculated to consider the entire period available (1958–2011) and just the period of the ECCO2 data reanalysis (1992–2011). The reanalysis and in situ data averages presented high correlation ($r \geq 0.8$) considering both time coverages for all layers and hydrographic properties ($\theta$, $S$, and $\gamma^n$). We decided to follow our analysis using the observational dataset restricted to the





OSD
11, 1023–1091, 2014



1992–2011 period to avoid possible biases because of decadal and lower frequency variability during the 50 year period.

To quantify how well the reanalysis data reproduce the observed Southern Ocean hydrographic properties, the similarity between the averaged fields was characterized in terms of statistical parameters regarding both datasets. Considering the regional differences of hydrographic properties and processes within the Southern Ocean, the study area was divided into five hydrographic sectors according to Cavalieri and Parkinson's (2008) definition: the Bellingshausen and Amundsen Sea (B&A), the Ross Sea, the Western Pacific, the Indian, and the Weddell Sea sectors (Fig. 1). In each sector, the correlation coefficient, centered root-mean-square (CRMS) difference, and standard deviations were computed for the previously defined layers (SL, IL, and BL) from both datasets and considering each hydrographic parameter ($\theta$, $S$, and $\gamma^n$). These statistical parameters are summarized in a Taylor (2001) diagram in which the observational field is considered as a reference ($R$). For each evaluated field, the CRMS difference and two standard deviations are normalized by the standard deviation of the corresponding reference field. In this way, the statistics from the different hydrographic properties and fields are nondimensionalized and can be presented in a single diagram. Reanalysis fields that are more consistent with observations will be located closer to the "reference" point. Those fields will present low CRMS differences and high correlations with the observed field. The closer the reanalysis standard deviation is to the observational standard deviation (in this case, the standard deviation from in situ data is equal to 1 because the data were normalized), the better the spatial patterns are represented.

Using the ECCO2 monthly fields corresponding to the occupation dates of WOCE sections SR2, SR3, and SR4, we selected the reanalysis grid points closer to the in situ observations. The datasets have different vertical resolutions, and the measurements positions change among occupations. To allow for a comparison, data from both datasets were averaged onto a regular grid and then averaged over time. The vertical resolution of the grid followed the depth levels from the reanalysis, whereas the





OSD
11, 1023–1091, 2014



horizontal resolution was 0.5° latitude (WOCE SR2 and SR3) and 1° longitude (WOCE SR4).

We calculated the percentage of area occupied by the AABW in each section and also the averaged $\gamma^n$ of this layer. Similar calculations were made by Fahrbach et al. (2004) and Renner et al. (2009) in the Weddell Sea. The averaged hydrographic properties from the occupations that did not extend to the entire section (WOCE SR2: March 1999, WOCE SR3: March 1996, and WOCE SR4: November 1992 and April 1998) were not directly compared with the results from other occupations to avoid bias resulting from the differences in properties along the sections. To allow a direct comparison between the ECCO2 and observational area estimates, the reanalysis data were restricted to the same depths and grid positions of the existing observational data. The same calculations were performed based on the complete reanalysis data available in both space and time.

### 2.4.2 Ocean current velocity and volume transport

The performance of the ECCO2 reanalysis in representing ocean current velocity and volume transport of dense water masses was evaluated in specific *case studies* based on the results and data presented by previous studies (e.g., Fahrbach et al., 2001, 2011; Klatt et al., 2005; Gordon et al., 2010; Fukamachi et al., 2010; Kerr et al., 2012). In all cases, even when the raw observational data were used (Klatt et al., 2005; Gordon et al., 2010), we seek to follow the original methodology as closely as possible to produce robustness for the reanalysis-observation comparisons.

The ECCO2 grid points that were closely positioned to the array of eight current-meter moorings on the eastern flank of the Kerguelen plateau (February 2003 to January 2005, Fukamachi et al., 2010; *Section* I in Fig. 1) were selected for reanalysis-observation comparison in the Indian Sector of the Southern Ocean. Following the method of Fukamachi et al. (2010), the reanalysis data along the section were vertically interpolated into 10 m bins from a 900 m depth to the bottom. The ocean current velocity components were rotated to the section orientation, and the cross-section





OSD
11, 1023–1091, 2014



component was used to determine the AABW volume transport that was integrated from the southwestern section limit to the zero crossing point from the northwestward to the southeastward transport. The AABW definition followed our previously defined threshold ($\gamma^n \geq 28.27\,\mathrm{kg\,m^{-3}}$) because the isotherm limit used by Fukamachi (2010) (waters colder than 0 °C) was not present in the reanalysis data section during the comparison period.

The M2 and M3 oceanographic moorings were deployed in 1999 at the continental slope of the South Orkney plateau and were equipped with two current meters (data available for 2000–2007): one at ~ 15 m and the other at ~ 500 m from the bottom (Fig. 1). More details on the mooring data can be found in Gordon et al. (2010). We selected the ECCO2 grid points closer to the mooring positions and extracted $u$, $v$, $\theta$, $S$, and $\gamma^n$ values from the depth level corresponding to the bottom current meters present at M2 (~ 3100 m, 2999 m in the reanalysis) and M3 (~ 4580 m, 4264 m in the reanalysis).

An array of moored current-meters along the Prime Meridian (between 69.5° S and 57° S) collected data from 1996 to 2000 (Klatt et al., 2005). Measurements from 2001 to 2008 from the same locations were added to this dataset (Fahrbach et al., 2011). The zonal velocity from the reanalysis data was extracted for the position of moorings M229 and M233 (Fig. 1), which were located at a depth of 2000 m. The former is located just north of Maud Rise, whereas the latter is immersed within the Antarctic Coastal Current near the Antarctic continental slope. A time series of reanalysis volume transport perpendicular to the section was determined based on the ECCO2 data points south of 60° S (*Section* IV in Fig. 1). This estimate was made considering the entire water column and just the AABW layer. In addition, we have computed the cumulative volume transport along the section and averaged it for both the period of the Klatt et al. (2005) dataset (1996–2000) and the entire reanalysis period.

To compare our results with those found by Fahrbach et al. (2001), we selected the ECCO2 grid points closer to the four current meter moorings maintained on the northwestern Weddell Sea (1989–1998; Fahrbach et al., 2001; *Section* II in Fig. 1). The data





OSD
11, 1023–1091, 2014



were interpolated onto a grid of 20 km horizontal resolution, and the velocity components were rotated to represent the currents perpendicular to the section. In Fahrbach et al. (2001), the WSBW volume transport time series was determined following the threshold of $\theta \leq -0.7\,^{\circ}\mathrm{C}$. Because our dataset does not present such a cold water mass during the analysis period, we determined the volume transport of the AABW ($\gamma^n \geq 28.27\,\mathrm{kg\,m^{-3}}$) to allow for comparison because the AABW properties are partly controlled by the WSBW formation (e.g., Orsi et al., 1999).

### 2.4.3 AABW variability

The variability of the AABW layer from observational and reanalysis data was evaluated by linear trends of annual time series from hydrographic properties. The AABW data from both datasets were averaged onto a 2° grid. This coarser resolution results from the scarcity of in situ data; therefore, grid cells might include measurements from different years. Annual averages were determined within each grid cell, which were also spatially averaged to determine an AABW annual time series for the entire Southern Ocean and regional sectors (empty bins were not considered in calculations). For the ECCO2 data, the sensitivity analyses of annual trends were determined based on all months of the years and the original grid resolution (0.25° × 0.25°).

The AABW volume change through the years was analyzed by determining the pentad volume anomalies. The top of the AABW layer was considered as having the shallowest occurrences of $\gamma^n \geq 28.27\,\mathrm{kg\,m^{-3}}$ in each grid point averaged for each four year period. The bottom of the layer was assumed to be the seabed. Bathymetric data were obtained from the ETOPO2v2 Global Gridded 2-Minute database (US National Geophysical Data Center, http://www.ngdc.noaa.gov/mgg/global/etopo2.html). The pentad AABW volume was then calculated as the integral from the upper boundary of the AABW to the seabed. The pentad anomalies were computed with reference to the 20 year average.





OSD
11, 1023–1091, 2014



## 3 ECCO2 Southern Ocean representation

### 3.1 Climatological representation of the Southern Ocean water masses

The ECCO2 and observational hydrographic properties were compared in a $\theta$–$S$ space in which the entire water column was evaluated. Twenty-year averaged (summer-only) $\theta$–$S$ diagrams were built using ECCO2 data in their original horizontal and vertical resolution. The observational dataset was averaged onto the reanalysis grid and time averaged again. Figure 2 shows the $\theta$–$S$ diagram for each Southern Ocean sector (as defined in Fig. 1). The bottom left panel of Fig. 2 shows the diagram based on the ECCO2 for the data averaged by area in each ocean sector.

The regional $\theta$–$S$ diagrams (Fig. 2) reveals that shelf waters are reasonably well represented by the reanalysis data, especially in the Weddell and Ross Sea sectors, where the near freezing, high salinity shelf waters are present. The AASW presents a wide property range because of its surface location (above 200 m depth) at the air–sea and ice interface (Whitworth et al., 1998). Fresher and colder AASW resulting from seasonal variability is not present in the reanalysis. The ISW, an important component of the AABW (Foldvik et al., 2004), is not represented either, which is expected because ice shelves are not considered in the model used for the ECCO2 data assimilation. Thermodynamic fluxes between the ice shelf and ocean are highly relevant for an adequate representation of the hydrography on the shelf region (Meccia et al., 2013). The $\theta$–$S$ diagrams including only water below 500 m (Fig. 2, inserted panels) show that the reanalysis maximum temperature and salinity are displaced toward lower absolute values for all sectors. Such a displacement generates cold and fresh intermediate water that is represented by the reanalysis data. The AABW is present in all sectors, although the colder and saltier variety from each sector is not represented (Fig. 2). One exception is the densest bottom water layer from the Weddell Sea (WSBW; $\gamma^n \geq 28.4\,\mathrm{kg\,m^3}$).

The ECCO2 averaged fields of $\theta$, $S$, and $\gamma^n$ for each defined layer (SL, IL, and BL) are presented in Fig. 3 along with the difference of the observational density field from the reanalysis estimates. The major oceanographic features are reproduced by





OSD
11, 1023–1091, 2014



the reanalysis data in all fields. The SL (Fig. 3a, see Supplement for high resolution figure) cold waters are present around the Antarctic continental shelf with values lower than −1 °C. The coldest water mass is seen in the southern Weddell Sea shelf (∼ −1.9 °C). Surface cold waters (below 0 °C) are also present in the Weddell Sea open ocean regime, which characterizes the Winter Water. A slightly higher temperature is noticed along the Antarctic continental shelf break because of the mixture of shelf waters with CDW that enters the Weddell Sea following the gyre circulation. The open ocean surface waters of the Western Pacific and Indian sectors present temperatures higher than 0.5 °C.

Shelf waters with high salinity ($S \geq 34.55$) are present in the Ross and Weddell Sea continental shelves, and waters saltier than 34.62 are concentrated in the western portion of these shelves regions. The spread of a high salinity plume is also noticeable from the Ross Sea until approximately 90° E. The open ocean region of the Weddell Sea is also filled with waters of salinity $S \geq 34.5$. Figure 3a shows the densest ($\gamma^n \geq 28.4\,\mathrm{kg\,m^{-3}}$) water masses in the south and southwestern portion of the Weddell Sea continental shelf and western shelf of the Ross Sea. Relatively less dense waters ($\gamma^n \sim 28.27\,\mathrm{kg\,m^{-3}}$) are present in the northwestern Weddell Sea shelf. Water masses with $\gamma^n$ of approximately $28\,\mathrm{kg\,m^{-3}}$ spread from the Ross Sea until they reach Prydz Bay. In accordance with the reported production of dense waters in the Adelie Land and Prydz Bay region, waters within this bay and along the coast of Adelie Land are denser than the surrounding waters. Waters with density ranging from 28.1 to $28.27\,\mathrm{kg\,m^{-3}}$ cover the WG region.

The averaged IL field presents $\theta \leq -1.5$ °C in the Weddell Sea, Ross Sea, and Prydz Bay continental shelves (Fig. 3b, see Supplement for high resolution figure). The IL involves the core of CDW. Thus, the open ocean regime of the B&A, Ross Sea, Western Pacific, and Indian sectors presents $\theta \geq 0.5$ °C, while the Weddell Sea $\theta$ values are relatively lower ($0\,^\circ\mathrm{C} \leq \theta \leq 0.5\,^\circ\mathrm{C}$). These differences are related to the temperature attenuation caused by mixing of the Winter Water and CDW as the latter flows along the WG (Weppernig et al., 1996), resulting in WDW, which is defined inside the Weddell basin.





OSD
11, 1023–1091, 2014



The Ross Sea presents the saltiest water masses of all the shelves ($S \geq 34.73$) and open ocean regions ($S \geq 34.7$). Waters with density ranging from 28.0 to 28.27 kg m$^{-3}$ occupy the Ross Sea, Western Pacific, Indian, and Weddell Sea open ocean regime as well as the coastal region of the B&A sector. An unusual feature is the presence of the 28.27 kg m$^{-3}$ isopycnal north of 66° S in the Weddell Sea open ocean regime.

The BL averaged $\theta$ field presents a dichotomic pattern, with waters colder than 0 °C from east of the Antarctic Peninsula until approximately 120° E and warmer water masses occupying the area from this region to west of the Antarctic Peninsula (Fig. 3c, see Supplement for high resolution figure). The coldest bottom waters are seen in the Weddell Sea. The lowest salinity values are found in the Weddell and Indian sectors ($S \leq 34.68$), the highest in the B&A and the Ross Sea sectors ($S \geq 34.7$). The Weddell Sea and western region of the Indian sectors present the densest bottom water masses ($\gamma^n \geq 28.3$ kg m$^{-3}$), which are the densest masses in the deep Weddell Basin. The Ross Sea and B&A sectors encompass waters lighter than $\gamma^n = 28.27$ kg m$^{-3}$ (the AABW threshold), which are limited to the Ross gyre region. These general features are consistent with the description by Orsi et al. (1999) of the differences in bottom waters between basins based on observational data, which describe the coldest and freshest bottom water masses in the southwestern Weddell Sea, the warmest and saltiest waters in the northwestern Ross Sea domain, and intermediate values in the Western Pacific sector.

Despite the good reproduction of the main oceanographic features by the ECCO2 reanalysis data, there are certain discrepancies regarding the absolute $T/S$ values that lead to differences between density fields. The reanalysis representation of the SL in the Southern Ocean is generally denser than observations, with local cases of density underestimation, such as in the western Ross Sea continental shelf (Fig. 3a). Misfits in the representation of surface waters can also be observed in the $\theta$–$S$ diagrams (Fig. 2), which are possibly the result of the reanalysis having difficulty reproducing the several complex processes acting on the ocean surface that are compounded in coastal waters by the absence of ISW. As a result of the colder and fresher intermediate layer





OSD
11, 1023–1091, 2014



(Fig. 2), the IL density is overestimated in most of the Southern Ocean (Fig. 3b). The exception is the B&A sector and circumpolar shelf regions. The BL density difference field (Fig. 3c) presents lighter deep water masses, which might have been caused by the general absence of colder and saltier bottom varieties of AABW (Fig. 2). This absence might have resulted from a bad representation of newly formed dense waters spilling off the shelf. Moreover, the coarse vertical grid resolution at greater depths implies that deep waters are represented by the average property of an approximately 400 m water column, which leads to the masking of the approximately 100 m thick bottom water layer. Along the Prime Meridian, the differences between fields are less than 0.01 $kg\,m^{-3}$.

Although differences in the absolutes values may occur, climatological averages of the reanalysis data provide a good representation of the Southern Ocean water masses and can reproduce the average shape of the $\theta$–$S$ diagrams from in situ data. However, the spatial distribution of the hydrographic properties through time (Fig. 4) suggests that the waters in most of the Southern Ocean are badly represented by the ECCO2 data during the last six years evaluated in this study (2006–2011) as a result of anomalous hydrographic property values. A dense plume at the SL appears in the 2006–2007 period (Fig. 4). In the last two years, waters with $\gamma^n \geq 28.4\,kg\,m^{-3}$ not only fill the deep basins of the Weddell Sea but also reach the surface and spread within the region. The AABW area estimates (see Sect. 3.2) show that abrupt changes in water masses can be identified since 2004.

To evaluate the effect of those anomalous years on the hydrographic properties of the climatological state, previously presented analyses were performed again considering only the period from 1992–2004 (not shown). For the SL, the main differences between averaged fields from the limited (1992–2004) and complete (1992–2011) periods are the warmer and fresher waters in the Weddell Sea and Indian sectors and the fresher waters flowing out of the Ross Sea. As a result, the surface waters are generally less dense. The $\gamma^n = 28.0\,kg\,m^{-3}$ and $\gamma^n = 28.1\,kg\,m^{-3}$ isopycnal are essentially limited within the Weddell Sea. The smaller differences between the reanalysis and





OSD
11, 1023–1091, 2014



in situ SL density fields are evident in the Weddell Sea and Indian sectors considering the restricted period. Unlike the SL, the IL level differences between periods can only be noticed in the Weddell and Indian sectors, where warmer and saltier waters are observed if the restricted period is considered. The differences between the reanalysis and observed temperature decrease in those sectors and becomes negative in the inner and northwestern Weddell Sea. As a result, the water represented by the reanalysis within the Weddell Sea becomes lighter than observations. The unusual plume of water denser than $\gamma^n = 28.27\,\mathrm{kg\,m^{-3}}$ close to the Prime Meridian is not present in the averaged field for the restricted period. The BL averages from both periods are similar. The most prominent difference is the lack of the $\gamma^n = 28.39\,\mathrm{kg\,m^{-3}}$ isopycnal, which leads to waters that are slightly lighter than observations. The $\theta$–$S$ diagrams from the different periods are also similar, although there is a greater volume of points with densities of $28.1 \leq \gamma^n \leq 28.4\,\mathrm{kg\,m^{-3}}$ in detriment to waters denser than $\gamma^n = 28.27\,\mathrm{kg\,m^{-3}}$ in the Weddell Sea and Indian Ocean sectors based on the 1992–2004 period. The mean differences of the hydrographic property fields reproduced by the reanalysis and observations in surface and intermediate layers are reduced by approximately 25 % and 21 %, respectively, if only the reliable period (1992–2004) is considered.

Taylor diagrams (Fig. 5) show that when only the restricted period is used, there is a decrease in the standard deviation of reanalysis data for the SL and IL because of the exclusion of the anomaly values of the most recent years. In contrast, the BL correlation coefficient is higher when the entire period is considered as a result of the cold and dense average of these water masses. However, the hydrographic representation of the most recent years (2004–2011) is inadequately performed by the ECCO2 reanalysis; therefore, this period is treated with caution in all further analysis.

The relative skill of the ECCO2 reanalysis in representing the $\theta$, $S$, and $\gamma^n$ fields in the defined layers (SL, IL, and BL) during the reliable period is summarized in a Taylor diagram. The hydrographic properties are not equally well represented between the sectors. The temperature statistics from the distinct sectors are similar and relatively close to the reference (Fig. 5a) in the SL. The Indian density field, in addition to the





OSD
11, 1023–1091, 2014



B&A salinity, comprises the poorest representation of the observed fields. Most of the sectors and properties underestimate the spatial variability of in situ data. The Ross Sea sector density field reveals the most consistency between reanalysis and observations in the SL layer. All other sectors and parameters have correlation coefficients less than 0.9. The best-represented fields in the IL are temperature from the Ross Sea, Indian, and Western Pacific sectors and density from B&A, which all present correlation coefficients greater than 0.9 (Fig. 5b). The salinity fields are the most poorly represented fields for all sectors. Every field and sector evaluated in the IL present a standard deviation less than 1, which indicates smaller amplitudes in the variation pattern when compared with in situ data. The BL field values are widely spread in terms of standard deviation, and salinity is the parameter with the lowest values (Fig. 5c). The temperature and density fields from the Ross Sea and B&A sectors are the most similar to the observational field.

### 3.2 Water mass representation along repeat hydrographic sections

To compare the hydrographic properties from in situ observations and reanalysis data along the historical sections (Fig. 1), only the period from 1992 to 2004 of the ECCO2 dataset was considered. The most recent years of the simulation had clear problems and affected the temporal average of the sections' properties, which led to misleading interpretations of the general reanalysis performance. Figure 6 (see Supplement for high resolution figure) shows the averaged ECCO2 temperature and salinity fields along the defined sections, the difference between reanalysis and observational density fields, and $\theta$–$S$ diagrams for each section. The isolines of $\theta = 0\,^{\circ}\mathrm{C}$ and $S = 34.64$ from both datasets are presented for comparison in the temperature and salinity fields, respectively. Several studies used these combined hydrographic thresholds to define the AABW limits (e.g., Wepperning et al., 1996; Meredith et al., 2000; Klatt et al., 2005), which generally coincide with the $\gamma^n = 28.27\,\mathrm{kg\,m^{-3}}$ threshold used in our study for the open ocean regime (e.g., Orsi et al., 1999; Kerr et al., 2012).





OSD
11, 1023–1091, 2014



In the context of WOCE, the goal of section WOCE SR3 was to monitor exchanges between the south Indian and Pacific Oceans (Rintoul, 1999). Only the southernmost portion of this section, extending from the shelf break to approximately 60° S just south of the polar front (~ 59° S), was evaluated. According to Rintoul (1999), there are two expressions of the polar front in the region of the southern branch marked by the northern extent of the 0 °C isotherm, as defined by Nowlin et al. (1977). The average temperature profile of section WOCE SR3 (Fig. 6a) indicates the extension of the 0 °C isotherm from in situ data until approximately 60° S in the upper ocean and along the entire section at greater depths. The 0 °C isotherm from the reanalysis, however, is absent in deep waters and presents a more restricted extension at the surface, although a minimum temperature (0–0.5 °C) is present along the section. The similarity of the reanalysis and observed averaged salinity profile (Fig. 6a) is evidenced by the 34.64 isohaline that reproduces the salinity increase in surface waters south of 62.5° S. However, the characteristic slight decrease of salinity with depth is not present. The differences between the reanalysis and observational averaged density profiles indicate an AABW layer lighter and narrower than expected and a denser intermediate water south of 63° S. The $\theta$–$S$ diagram (Fig. 6a) shows fresher and colder intermediate waters, which can lead to the density overestimation noted in Fig. 6a. A lighter representation of this water mass in the northern part of the section (Fig. 6a) is related to greater salinity differences between the two datasets. This change from positive to negative density anomalies coincides with the southern limit of the eastward transport ("southern ACC front") identified by Orsi et al. (1995) as a front located south of the polar front that is usually marked by the southernmost extent of maximum temperatures. Rintoul (1999) identified this front at approximately 63° S, which coincides with the front location in the reanalysis temperature profile. Thus, the observed change in density representation may be linked to a dynamical barrier, with northern (southern) waters lighter (denser) than expected. The $\theta$–$S$ diagram (Fig. 6a) also indicates that reanalysis bottom waters do not reach the minimum in situ temperatures; they present a smaller slope in the mixture line from intermediate to deep waters and have almost





OSD
11, 1023–1091, 2014



the same salinity down to the bottom. These differences contribute to the generation of a lighter and narrower reanalysis of the AABW layer, which is indicated by the negative differences shown in Fig. 6a and the deeper 28.27 kg m$^{-3}$ isopycnal. Therefore, the AABW volume in this region is lower than expected and supplied primarily by the relatively warmer and saltier bottom water from the Ross Sea because the colder and fresher Adelie Land Bottom Water is absent.

The eastern and western portion of the WOCE SR4 repeat section crosses the inflow and outflow regions of the inner Weddell Sea. Section WOCE SR2 captures the waters entering the Weddell Gyre for further modification by the ice/ocean/atmosphere interaction and the dense waters recirculating within the gyre. The property fields of the sections within the Weddell Sea and along the Prime Meridian are consistent between the reanalysis and in situ data, as indicated by the highly coincidental 0 °C isotherm and 34.64 isohaline (Fig. 6b and c). Consequently, the upper AABW limit is also well represented in both sections. The major regional features are represented by the reanalysis data, e.g., the characteristic doming of the Weddell Sea cyclonic gyre (Fahrbach et al., 2004), which is noticeable north of 64° S at section WOCE SR2. Cold and fresh surface waters overlay the WDW temperature and salinity maxima, and below this depth, $\theta$ decreases to the bottom. The signature of the Antarctic slope front is also present in both sections; it is defined as a cold and fresh flow around Antarctica (Gill, 1973) and was identified by Jacobs (1991) as the shoreward extent of the 0 °C isotherm corresponding to the downward slope of the isotherm. The warm core of the WDW proximal to the continental shelf is well defined in the reanalysis data for both the WOCE SR4 and WOCE SR2 sections. However, the temperature of the WDW flowing into the Weddell Sea (eastern WOCE SR4 and southern WOCE SR2; greater than ~ 0.6 °C for in situ data) is lower than expected, whereas the outflowing water (western WOCE SR4; ~ 0.4 °C for in situ data) is warmer. This feature is also evident in the averaged IL (Sect. 3.2), suggesting that the cooling process that should occur within the gyre is not as efficient in the model, leading to waters that are warmer than expected, not only in the observed





OSD
11, 1023–1091, 2014



intermediate levels but also in the deep waters recently formed in the region (Figs. 3 and 6).

Despite the good representation of the 0 °C isotherm, the slope of the temperature decrease from this deep isotherm to the bottom of the ocean is not as pronounced (Fig. 6b and c) and leads to a representation of bottom waters that does not reach the WSBW temperature threshold (−0.7 °C) or corresponding neutral density (28.4 kg m$^{-3}$). Consequently, the bottom layer is lighter in both sections (Fig. 6b and c, panel $\gamma^n_{\mathrm{diff}}$). In WOCE SR4, a lighter representation of the water masses extends to approximately 100 m in depth and is also related to higher temperatures (Fig. 6b, panel $\gamma^n_{\mathrm{diff}}$). The denser water in the western end of WOCE SR4 is not associated with a dense downward flow along the slope but is rather a result of saltier waters from 100–300 m (south of 34.64 isohaline) and a slightly cold water core from 400–1500 m (also visible by the 0 °C isotherm, which does not reach the same slope in the reanalysis as it does the in situ data).

The difference between the intermediate waters in the sections appears in the $\theta$–$S$ diagrams (Fig. 6b and c). In WOCE SR2, the colder and fresher representation of intermediate waters is more evident because this section primarily includes the inflowing WDW, whereas WOCE SR4 also includes the water exiting from the Weddell Sea, which seems slightly warmer than expected. Figure 6 shows that the reanalysis data do not present the colder and fresher variety of the AABW in those sections for the periods evaluated. In both repeat sections, the absence of the denser AABW variety (WSBW) may be compensated by the WSDW. For section WOCE SR3, however, the 28.27 kg m$^{-3}$ isopycnal is deeper.

Figure 7 presents the estimates of the area occupied by the AABW layer along sections and the average upper limit and density of this dense layer. The estimates based on reanalysis data that are restricted to the in situ data availability (gray circles in Fig. 7) and estimates based on complete data coverage (black line in Fig. 7) are generally similar. Thus, the differences in spacing between station occupations have not strongly affected the results. However, incomplete section occupations have stronger effects on





OSD
11, 1023–1091, 2014



the estimates because in these cases, there are greater differences between estimates from restricted and complete ECCO2 data. In general, for occupations before 2004, the reanalysis data underestimates the AABW area and average density and overestimates the upper limit depth. Greater differences of the AABW area and upper limit depth are found in WOCE SR3, which was expected because the 28.27 kg m$^{-3}$ isopycnal was deeper than expected in the averaged section (Fig. 7a). Sections WOCE SR2 and SR4 (Fig. 7b and c, respectively) present similar estimates from both datasets during that period, with differences between area estimates up to 6 %. Another different aspect from the section in the Western Pacific and sections within the Weddell Sea is that the former presents much more pronounced temporal variability.

The WOCE SR3 time series (Fig. 7a) does not present abrupt changes in any of the estimates. After 2002, however, the averaged AABW upper limit depth decreases, whereas the area occupied by this layer is smaller than in the previous years. This change suggests that the AABW layer became shallower but decreased in extent along the SR3 section during the second half of the time series. Section WOCE SR2 (Fig. 7b) shows an unrealistic change in the area (from ~ 66 % to ~ 90 %) and depth (from ~ 1500 m to ~ 480 m) of the AABW that remains until the end of the simulation and results from the dense plume that appeared after 2004 (Fig. 4). The average density also increases and presents a marked seasonal signal in the end of the series. In February 2005, there is a decrease (increase) of the AABW area (depth), which is possibly because of the assimilation of in situ data during that time. After that, the AABW area (depth) increases (decreases) and stabilizes at the end of 2006 to occupy most of the water column. After March 2008, the entire AABW layer is composed of water denser than 28.4 kg m$^{-3}$. Concurrently, the AABW stabilizes in WOCE SR2 and the AABW area and density (depth) begin to increase (decrease) in pulses in section WOCE SR4 (Fig. 7c). In the last two years of the dataset (2010–2011), this dense water fills almost the entire water column. Clearly, in situ data do not show that pattern. Mean differences between estimates from the distinct datasets are ~ 16 and ~ 4 times higher during the most recent years for sections SR2 and SR4, respectively. Finally,





OSD
11, 1023–1091, 2014



these results are consistent between area estimates from the reanalysis and observational datasets throughout the time series but confirm the inability of the ECCO2 to reproduce hydrographic properties and structure beyond 2004.

### 3.3 Velocity and volume transport assessment

The assessment of the AABW current velocity and volume transport variability is performed in four *case studies* based on data previously reported in the literature, and each case study is highlighted below.

#### 3.3.1 Case study I: Kerguelen Plateau/Indian sector

The Kerguelen Plateau deep western boundary current was recently identified as a significant pathway of deep water transport from the Southern Ocean toward lower latitudes. This region (Fig. 1) is characterized by a narrow and intense northwestward flow close to the plateau and a southeastward flow offshore (Fukamachi et al., 2010; hereafter referred to as F10). Figure 8a presents the ocean current velocity field of the ECCO2 reanalysis data for *Section* I, which is located east of Kerguelen Plateau. The reverse flow at approximately 110 km from the southwestern section limit (defined at −58.12° S, 82.62° E for the ECCO2 data) is noticeable. The F10 study defined the AABW as bottom waters with $\theta < 0\,^{\circ}\mathrm{C}$ that reach approximately −0.35 °C at the bottom layer. As previously noted, the bottom waters represented by the ECCO2 dataset are warmer than expected (Figs. 2 and 3) and do not reach those temperature values at the seabed (Fig. 8a). Notably, in section WOCE SR3, the isotherm $\theta = 0\,^{\circ}\mathrm{C}$ is absent in the deep ocean, which is in contrast with the observations (Fig. 6). However, the ECCO2 $28.27\,\mathrm{kg\,m^{-3}}$ $\gamma^n$ isopycnal coincides in depth with the F10 0 °C isotherm throughout the section. Thus, the AABW layer is reasonably defined with a thickness of approximately 1500 m in the ECCO2 reanalysis (Fig. 8a).

The cores of northwestward and southeastward AABW flow are located approximately 75 km and 165 km, respectively, from the southwestern section limit (Fig. 8a).





OSD
11, 1023–1091, 2014



Despite the similarities of the general structure of the deep and bottom current velocity from the ECCO2 and F10 mooring fields, the ECCO2 average velocity absolute values are considerably lower than observations (for example, F10's Fig. 2). The ECCO2 deep western boundary current mean transport of 3.7 ± 1.3 Sv (Fig. 8b) for the observed period (February 2003 to January 2005) is much lower than the 12.3 ± 5.6 Sv estimate based on the F10 moorings data. The reanalysis data do not seem to represent the observational variability pattern because the correlation between time series is low ($r = -0.2$). The rugged bathymetry and poor model spatial resolution can contribute to the difficulty of reanalysis data in reproducing the deep and bottom volume transport variability. Since 2006, there has been a continuous increase in the AABW flow (Fig. 8c), leading to an AABW transport of 12 Sv at the end of the series, which is close to the mean flow reported by F10 (i.e., 12.3 Sv). However, these years with higher AABW transport coincide with the period during which ECCO2 produces unreliable hydrographic conditions.

### 3.3.2 Case study II: Endurance ridge/Weddell Sea sector

The deep and bottom water properties at the northern limb of the Weddell Sea were evaluated by Gordon et al. (2010) and Mckee et al. (2011) using data from bottom moorings M2 (3096 m; 62°38′ S; 043°15′ W) and M3 (4560 m; 63°32′ S; 41°47′ W) (Fig. 1). The latter is associated with the eastward flow of the WSBW originating in the southwestern Weddell Sea, whereas measurements from M2 are related to the WSDW formed further north.

In this *case study*, the monthly velocity time series of the deepest current meters from each mooring are compared with current velocity time series from the ECCO2 at approximately the same depths (Fig. 9a–c). The time series are well correlated in both moorings ($r = 0.58$ for M2 and $r = 0.57$ for M3). Seasonal fluctuations are quite clear in the time series from both datasets and are possibly linked to the seasonal cycle of the winds over the western margin of the Weddell Sea (Gordon et al., 2010). The amplitude of seasonal variations is higher in the time series from observational





OSD
11, 1023–1091, 2014



data and more evident at M3. The different time series patterns of variability might be related to distinct water mass sources and forcing of the water flowing through each mooring.

In general, the average current velocities from reanalysis data are lower than observations, despite the similarity present during the low-current velocity periods at M3. There is an increasing trend in the ECCO2 reanalysis velocity time series that leads to values close to the in situ average ($\sim 12\,\mathrm{cm\,s^{-1}}$) in July 2007 at M3. From that point on, the velocity from M3 increases more abruptly, whereas M2 reanalysis velocities decay until they reach the previous mean values. The ECCO2 density time series at the moorings locations (Fig. 9d) reveal an interannual variability, although the seasonal cycle is not so evident.

The latter is associated with the eastward flow of the WSBW originating in the southwestern Weddell Sea, whereas measurements from M2 are related to the WSDW formed further north.

Although the M3 is associated with the WSBW flow, the extracted reanalysis data do not reach the WSBW observed density (Fig. 9d). However, the simulated bottom layer is denser than the variety found at the M2 position, and both are denser than $\gamma^n = 28.27\,\mathrm{kg\,m^{-3}}$.

### 3.3.3 Case study III: Prime Meridian/Weddell Sea sector

Also within the Weddell Sea sector is a moorings array along the Prime Meridian that was evaluated by Klatt et al. (2005), which is hereafter referred to as K05. The zonal current velocity from the reanalysis data was extracted for the position of moorings M229 (2007 m; 64° S and 0° E) and M233 (1950 m; 69.4° S and 0° E) (Fig. 1). The M229 velocity values from the datasets are similar, with ECCO2 mean values of $-3.21 \pm 2\,\mathrm{cm\,s^{-1}}$ and K05 of $-2.8 \pm 2.4\,\mathrm{cm\,s^{-1}}$ (Fig. 10a). At M229, the correlation between the time series from different datasets is low ($r = 0.1$), and if present, the seasonal cycle is dominated by higher frequency signals that are possibly linked to the proximity of the Maud Rise.





OSD
11, 1023–1091, 2014



At the M233 location, the absolute values are only similar during the weaker phases (December–January) of observational data (Fig. 10b). After 2007, there is an abrupt increase in velocity values from the ECCO2 data at the M233 position, which leads to mean values of $-12.7 \pm 1.5\,\mathrm{cm\,s^{-1}}$. This velocity is much higher than the previously average found in the ECCO2 time series ($-2.6 \pm 1.9\,\mathrm{cm\,s^{-1}}$) and also from observational mean values ($-4.5 \pm 2.4\,\mathrm{cm\,s^{-1}}$). The variability pattern is well correlated at M233 ($r$ = 0.68), with a clear annual cycle found in both time series.

According to K05, higher velocity values are found at M233, which is immersed in the Antarctic Coastal Current. The ECCO2 reanalysis velocity data do not follow this pattern because currents at M233 are weaker than at M229 before 2004.

Because the Weddell Sea Prime Meridian area is an intensively studied region (e.g., Schroder and Fahrbach, 1999; Farbarbach et al., 2004; Klatt et al., 2005; Kerr et al., 2009), we determined the transport of the entire water column south of 60° S (*Section* IV; Fig. 10c). In this estimate, the seasonal signal is not as evident as in the current velocity time series (Fig. 10a and b). However, the transport time series of the entire water column presents an intra-annual variability associated with a decreasing trend ($0.81\,\mathrm{Sv\,yr^{-1}}$) from 1992 to 2004 (Fig. 10c). From 2004–2007, there is also a strong reduction of the mean seasonal cycle amplitude (~ 23 %). Despite the decrease in the volume transport of the water column, the estimates for the AABW layer (average volume transport of ~ 19 Sv) do not present an evident trend from 1992 to 2004 (Fig. 10c), which means that during this period, the contribution of the AABW layer to the total volume transport south of 60° S increased. In July 2004, the AABW transport intensifies, increasing the variability range. After 2008, a stabilization is noted, with a mean transport of approximately $40\,\mathrm{Sv} \pm 23$. The contribution of the AABW to the cross-section volume transport increases from approximately 38 % at the beginning of the time series to approximately 80 % in the latter years.

Despite the high variability of the transport time series, the cumulative transport along the section (Fig. 10d) is comparable to that presented by K05, in which three major areas are observed (the Antarctic Coastal Current, a recirculation to the south





OSD
11, 1023–1091, 2014



of the Maud Rise, and westward current to the north of this bathymetric feature). The ECCO2 estimates based only on the period evaluated by K05 (1996–2000) show that the absolute volume transport of the southern limb of the Weddell Gyre is 51.7 Sv (Fig. 10d), which is similar to the transport of 56 ± 8 Sv determined by K05. The Antarctic Coastal Current in the ECCO2 data is less intense (absolute transport of 19 Sv) than the K05 estimates (26 ± 4 Sv), and the recirculation south of Maud Rise is absent or extremely weak. The cumulative transport of the AABW layer is ∼ 21 Sv for the southern Weddell Gyre (Fig. 10d), which is in contrast with the value of 28 Sv found by K05.

When the entire ECCO2 period is considered (1992–2011), the structure of the cumulative transport along the section is closer to observations because the Antarctic Coastal Current is better defined and because the recirculation south of Maud Rise is present (Fig. 10d). In this case, the absolute transport for the southern portion of the gyre is slightly increased (absolute transport of ∼ 54.4 Sv compared with ∼ 51.7 Sv for 1996–2000) and closer to the observational estimates. This increase is partially a result of a stronger Antarctic Coastal Current (absolute transport of 31.4 Sv) overestimating the previous estimate (19 Sv considering 1996–2000) and observations (26 ± 4 Sv). In the AABW cumulative transport, the distinct areas described above are also better defined when the entire period is considered. However, absolutes values are overestimated (absolute transport of 34 Sv for the southern limb of the Weddell Gyre; Fig. 10d) compared with the K05 results (28 Sv). If the K05 estimate for the AABW absolute transport for the southern limb of the Weddell Gyre is compared with the time series from the ECCO2 presented in Fig. 10c, it shows that the average transport after 2007 (∼ 39±11 Sv) is considerably higher than the observation.

### 3.3.4 Case study IV: Western Weddell Sea/Weddell Sea sector

Fahrbach et al. (2001) (hereafter referred to as F01) evaluated the export of newly formed dense bottom waters toward the northern limb of the Weddell Gyre using a mooring array at the northern tip of the Antarctic Peninsula (*Section* II; Fig. 1). The −0.7 °C isotherm used by the authors to define the bottom layer is not found in





OSD
11, 1023–1091, 2014



the similar ECCO2 transect evaluated during the period of F01 study (1992–1998); therefore, we performed the calculations based on the AABW layer defined here (Sect. 2.3). Figure 11a compares the ECCO2-estimated AABW volume transport with those determined by the F01 observational study and Kerr et al. model study (2012), hereafter referred to as K12. The absolute transport values from the ECCO2 and observational data differ because the dense layer definition used here is different from the F01 study, whereas the time series present a good temporal correlation ($r$ = 0.52 between the ECCO2 and F01). The observational transport increases after 1994 from an average value of 3.5 ± 0.6 Sv prior to this year to 3.9 ± 0.5 afterwards. An increase in absolute transport after 1994 is also present in the ECCO2 time series (from 2.3 ± 0.19 Sv average to 8.5 ± 3.4 Sv). The volume transport estimates based on the OCCAM model evaluated by K12 show absolute values that are higher than the reanalysis estimates despite the same AABW layer definition. Model variability estimates follow the same pattern of observations, as discussed by K12.

There is marked seasonal and interannual variability in the monthly time series of cross-*Section* II volume transport based on the ECCO2 data (Fig. 11b). As described by Fahrbach et al. (1995), the AABW flow has a well-defined seasonal cycle in which weaker flows occur in January and stronger flows occur in June. The months of maximum and minimum ECCO2 transport are consistent with estimates based on the OCCAM model (Kerr et al., 2012) but lag by one month from those determined by Fahrbach et al. (2001) (December and May), which suggests that both models and reanalysis have similar limitations in reproducing the AABW export variability. The average AABW flow found in the ECCO2 at *Section* II is 7.6 Sv with a seasonal range of ±2.5 Sv (Fig. 11b). This estimate is close to the volume transport of 6.7 ± 1 Sv and approximately 9 Sv determined by Naveira Garabato et al. (2002) and Franco et al. (2007), respectively, for WSDW exported over the South Scotia Ridge. The decrease of the AABW volume transport after 2005 from the ECCO2 estimates is not caused by stagnation of the dense water export but rather by the existence of a volume transport in the opposite direction in part of the section evaluated (not shown).





OSD
11, 1023–1091, 2014



Negative transport values are present until February 2010, after which a change in direction and substantial increase are observed until the end of the period analyzed. For most of the studied period, only WSDW contributed to the AABW volume transport estimated from the ECCO2 (Fig. 11b). However, episodic events of the direct injection of WSBW in the bottom layer (December 1998 to March 2000; April 2003 to September 2008; November 2010 to December 2011) increased the total volume transport. From 2003–2008, the ECCO2 average WSBW transport (1.86 Sv) was in accordance with that reported by F01 ($1.3 \pm 0.4$ Sv). In the most recent event of direct WSBW injection (November 2010 to December 2011), transport estimates were high, reaching approximately 20 Sv at the end of the time series, which corresponds to almost the totality of the AABW transport. The bottom current velocity annual averages (Fig. 11b) present a variability pattern similar to that of the volume transport time series. Although *Section* II is located north of a bottom water formation area, the origin of this dense bottom water is from southern regions; therefore, the variability of dense water transport must be affected not only by newly formed bottom water but also by remote thermohaline and wind forcing (Fahrbach et al., 2001). Kerr et al. (2012) show that the AABW export represented by OCCAM is primarily determined by the strength of the Weddell Gyre and its wind forcing, which is expected to occur in the ECCO2 reanalysis model.

The cross-shelf break ECCO2 bottom layer transport was determined in the northwestern Weddell Sea to evaluate the ventilation of the AABW to the deep Southern Ocean. The meridional section used for calculations is located just east of the 1000 m isobath (along the longitude 305°) and extends from 72° S to 65° S (~ 750 km; *Section* III – Fig. 1). The vertically integrated cross-section volume transport averaged for the entire study period (Fig. 12a) presents spatial patterns similar to the results of Muench and Gordon (1995) in which the southern and northern section ends are dominated by westward (negative) and eastward (positive) flow, respectively.

The volume transport time series for the AABW (deep and bottom dense water varieties; $\gamma^n \geq 28.27\,\mathrm{kg\,m^{-3}}$) and just the WSBW (bottom variety; $\gamma^n \geq 28.4\,\mathrm{kg\,m^{-3}}$) present a marked seasonal cycle (Fig. 12c). The AABW production occurs primarily in pulses





OSD
11, 1023–1091, 2014



(Schroder et al., 2002) that can be seen in the ECCO2 time series during three episodic periods (1994–1999, 2000–2004, and 2008–2011). The first two events coincide with the AABW production periods determined from the OCCAM simulation (Kerr et al., 2012). During the last event of the AABW production, the flow intensifies, reaching a maximum of 3.6 Sv (positive values for the east, i.e., offshore). The WSBW volume transport also intensified in the last production pulse (2008–2011) and reaches 1.9 Sv (Fig. 12c). Considering the entire period, the average volume transport estimates for the AABW and WSBW are $0.47 \pm 0.72$ Sv and $0.15 \pm 0.32$ Sv, respectively. If the period is restricted to 1992–2004, the average production rates of the AABW and WSBW decrease to $0.25 \pm 0.25$ Sv and $0.06 \pm 0.12$ Sv, respectively. In all cases, the volume transport estimates for both water masses are underrepresented compared with the $1.1 \pm 0.5$ Sv bottom water ($\theta \leq -0.7\,^{\circ}$C) formation rate estimated by Huhn et al. (2008) in the same area. This reduced spilling of dense flow of the AABW from the shelf may be related to the spatial resolution of the model used to create the reanalysis product, limiting the representation of coastal processes and coupled atmosphere–ocean–ice interactions. Moreover, the diffusion scheme generally applied in z-level global circulation models could also be a factor. Heuze et al. (2013) state that in typical diffusion schemes applied in z-level models, the dense water formed in the shelf region mixes horizontally and vertically when flowing down the slope; therefore, the dense signal is lost along the downward flow as a result of mixing with intermediate waters.

The ECCO2 estimates of absolute AABW volume transport in this meridional section (*Section* III; Fig. 12c) are lower than those found for the section perpendicular to the bathymetry (*Section* II; Fig. 11b) because the flow is predominantly northward along the shelf (Muench and Gordon, 1995). The WSBW transport from the ECCO2 is detectable in the northern section (*Section* II; Fig. 11b) only in specific periods that coincide with stronger WSBW outflow in the meridional section (*Section* III; Fig. 12c). During weaker flows, this signal may be lost by mixture along the northward displacement.

The time average of density fields along *Section* III (Fig. 12b) shows denser water masses on shallower regions near the edges of the section. The average upper AABW





OSD
11, 1023–1091, 2014



limit is determined based on the entire period and is also restricted to years before and after 2004. The upper AABW limit before and after 2004 (Fig. 12b) shows that dense water production increases during the most recent years (Fig. 12c) and does not affect the shelf water masses in the northern portion of the section. However, the area occupied by this water mass in the southern half greatly increases. The averaged AABW limit for the reliable period (1992–2004) shows that dense water spilling off the shelf is concentrated in the northern half of the section and follows the north and south slopes.

The *case studies* reveal that in the most important regions of the AABW export, the variability of volume transport and current velocity time series is well represented by the ECCO2 reanalysis data. In summary, the results obtained from *Section* I (located near the Kerguelen Plateau) reveal that the rugged bathymetry can be an important factor that contributes to the difficult task of reproducing the AABW volume transport variability in the Indian sector of the Southern Ocean. Despite the consistency in terms of variability, the absolute AABW current velocity and volume transport in all cases analyzed are underestimated by the ECCO2 before 2004. In addition to the bathymetry definition, the model spatial resolution and model diffusive scheme can also hamper the representation of dense deep and bottom water export from Antarctic shelves. From 2004 to 2007, there is an apparent adjustment of the reanalysis to different forcing conditions. After that, the AABW current velocity and volume transport overestimate the observations and, as discussed before, present unrealistic hydrographic conditions.

For the next sections, the results focus on the years from 1992 to 2004 and do not discuss the period of erroneous representation of the AABW variability (beyond 2004).

### 3.4 AABW variability

Four-year spatial averages of the AABW layer thickness and volume through time can be observed in Fig. 13a and b. At the beginning of the analyzed time period (1992–1995), the AABW layer represented by the ECCO2 (Fig. 13a) shows a geographical distribution that is similar to, though slightly thinner than, the 20 year averaged





OSD
11, 1023–1091, 2014



observational dense layer (Fig. 13c). Over the next decade (1996–2003), no visible changes in the dense layer thickness in the Weddell Sea, Indian, and Western Pacific sectors are evident (Fig. 13a).

A retreat of the dense deep layer in the B&A and Ross Sea sectors can be clearly seen throughout the AABW thickness and volume anomaly (Fig. 13a and b). By the 2004–2007 period, the AABW from the Ross Sea and B&A sectors is restricted to the core of the Ross Gyre. A contraction of the AABW layer from the 1980s to 2000s was recently reported by Purkey and Johnson (2012), who noted that the Australian-Antarctic and Amundsen-Bellingshausen basins present the highest isopycnal deepening rates ($-13.2 \pm 6.7\,\mathrm{m\,yr^{-1}}$ and $-11.4 \pm 2.9\,\mathrm{m\,yr^{-1}}$, respectively). A volume decrease of dense waters is also reported by Azaneu et al. (2013), who show a $-8.06 \pm 0.38\,\mathrm{m\,yr^{-1}}$ average AABW upper limit rate of change for the period 1958–2010. Despite the significant retreat of the AABW layer in the ECCO2 data during the 1992–2004 period, the average deepening rate of the AABW isopycnal from the reanalysis data ($-3.06 \pm 1.81\,\mathrm{m\,yr^{-1}}$) is lower than the observational estimates determined by Purkey and Johnson (2012) and Azaneu et al. (2013). The overestimation of the AABW layer thickness present in 2004–2011 is a consequence of the dense bottom water injection in the Weddell Sea, as previously discussed.

The Southern Ocean AABW annual time series (summer only) of hydrographic properties from the ECCO2 and in situ historical data is presented in Fig. 14a (see Supplement for high resolution figure). The observational time series presents high interannual variability, in contrast with the monthly and annual averages from the ECCO2 data. Variations in observational data are naturally expected; however, such variation might be partially the result of an unequal geographical distribution of data throughout the years (Azaneu et al., 2013). Although the ECCO2 data do not show significant interannual variability, the annual means from the reanalysis and in situ time series coincide several times during the analyzed period for all hydrographic properties. The statistical correlations between the reanalysis and observational time series are 0.60, 0.36, and −0.02 for density, salinity, and potential temperature, respectively,





OSD
11, 1023–1091, 2014



(considering only the period when the hydrography is well represented, 1992–2004). The AABW temperature presents a low and negative correlation because it shows a cooling trend ($-0.0036\,^{\circ}\mathrm{C\,yr^{-1}}$) in the ECCO2, which is in contrast to the warming noticed in the observational data ($0.0020\,^{\circ}\mathrm{C\,yr^{-1}}$). However, salinity and density follow the observed variability pattern. The observational data show $-0.0009\,\mathrm{yr^{-1}}$ and $0.0011\,\mathrm{kg\,m^{-3}\,yr^{-1}}$ salinity and density change rates, respectively. The ECCO2 data present a similar salinity decreasing trend ($-0.0007\,\mathrm{yr^{-1}}$) and lower density changing rate ($-0.0001\,\mathrm{kg\,m^{-3}\,yr^{-1}}$). Trends from the reanalysis data are statistically significant for all parameters; however, none of the trends for observational data are significant. Sensitivity analyses of the annual averages for all months and the original reanalysis spatial resolutions are not significantly different from the temporal trends presented above. Azaneu et al. (2013) evaluated an extensive observational dataset (1958–2010) under different methodologies; after attenuating the effect of data distribution, they found an AABW warming of $0.0015\,^{\circ}\mathrm{C\,yr^{-1}}$ and a density decrease of $-0.0005\,\mathrm{kg\,m^{-3}\,yr^{-1}}$ for the entire Southern Ocean. Therefore, only the ECCO2 density trend is consistent with the observations.

The regional AABW time series show different rates of change for each Southern Ocean sector (Fig. 14b, see Supplement for high resolution figure; note that the time series of the Weddell Sea and Indian sectors are presented following the figure's right axis for improved visualization). During the first period (1992–2004), all sectors experience warming, freshening, and density decreases, excluding the Weddell Sea sector. This region warms until 2000 ($0.0028\,^{\circ}\mathrm{C\,yr^{-1}}$) before becoming colder and fresher.

The warming of deep and dense bottom waters has been previously reported within the Weddell Sea (1989–1995) and in the region of the Prime Meridian (Fahrbach et al., 2004). Freshening of the AABW occurs in the Indian and Pacific sectors of the Southern Ocean (1995–2005; Rintoul, 2007) along with temperature and salinity decreases of the Adelie Land Bottom Water along 140° E (1995–2005; Aoki et al., 2005). Azaneu et al. (2013) estimated an AABW average temperature, salinity, and density trend of $0.0015\,^{\circ}\mathrm{C\,yr^{-1}}$, $-0.0002\,\mathrm{yr^{-1}}$, and $-0.0005\,\mathrm{kg\,m^{-3}\,yr^{-1}}$ (1958–2011),





OSD
11, 1023–1091, 2014



although freshening is not a clear pattern throughout the Southern Ocean. The Southern Ocean sectors average changing rates of 0.0023 °C yr$^{-1}$, −0.0002 yr$^{-1}$, and −0.0007 kg m$^{-3}$ yr$^{-1}$ for temperature, salinity, and density, respectively, as determined with the ECCO2 data (considering the 1992–2004 period), are consistent with those found by Azaneu et al. (2013). Considering these average rates, the cooling trend presented by the entire Southern Ocean time series (Fig. 14b) is not entirely representative of the overall warming trend. The difference between estimates of property changing rates based on the average of the AABW properties from the entire Southern Ocean (Fig. 14b) and those based on the average of the sector trends is partially caused by the Weddell Sea cooling trend, which is the primary region contributing to the AABW layer. Therefore, the averaged Southern Ocean AABW property is influenced by changes in this region. This differs from the second case, in which each sector has the same weight in the trend calculation, so warming is prevalent. In addition, the contraction of the AABW layer in the B&A and Ross Sea sectors is an important factor leading to the overall cooling trend (Fig. 14a). Those regions present the warmer AABW variety, and its reducing contribution over time leads to reduced temperature average values for the entire Southern Ocean.

### 3.5 Sea ice and wind stress in ECCO2

To better understand the AABW variability, the sea ice-covered area and ice thickness data from the ECCO2 are evaluated. Monthly time series of the ECCO2 sea ice-covered area and sea ice thickness are shown in Fig. 15a (upper and bottom panels; see Supplement for high resolution figure). During winter seasons, when the sea ice concentration is at its maximum, data from reanalysis largely overestimate the satellite data by more than 20 % (Fig. 15a). During summer periods, the difference between reanalysis and satellite data is lower than approximately 5 %. There is a reduction in the maximum values of sea ice concentration from the reanalysis for 2001–2004, with a clear decreasing trend after that period. The trend of the reanalysis of sea ice concentration for the complete time series is −0.78 % yr$^{-1}$. The minimum sea ice concentration





OSD
11, 1023–1091, 2014



values also decreases through years. Those reductions in sea ice minimum and maximum concentrations from the ECCO2 over time lead to a highly coincidental reanalysis with the remotely measured sea ice-covered area time series in the most recent year of the comparison period (2010). Sea ice thickness time series from the ECCO2 (Fig. 15a) also present a similar decreasing trend ($-0.01\,m\,yr^{-1}$).

The exaggerated seasonal variability presented in the ECCO2 sea ice concentration and sea ice thickness time series can be related to the configuration of the coupled sea ice model. The sea ice model is based on zero-layer thermodynamics that assumes that sea ice does not store heat (Adcroft et al., 2012). Furthermore, the warmer surface water shown in Fig. 2 can be linked to the sea ice representation. During summer months, the sea ice concentration is close to reality and enables heat uptake by the ocean through solar radiation. In turn, the high values in winter can reduce the ocean heat loss to the surface and result in warmer surface waters (e.g., Renner et al., 2009). The reduction of maximum sea ice concentrations in the 2001–2004 period may have triggered the initial decrease of temperature and salinity in the Weddell Sea deep waters (Fig. 14b).

The annual anomalies of sea ice concentration (Fig. 15b, see Supplement for high resolution figure) show a decreasing trend for these parameters after 2002, leading to below average values for the entire Southern Ocean at the end of the time series. However, the main feature presented in the ECCO2 sea ice field is the opening of an open ocean polynya east of the Prime Meridian in 2005, which leads to the retreat of sea ice in the following years (Fig. 15b). The lowest sea ice coverage occurs in 2010, followed by a slight recovery in 2011. Therefore, sea ice coverage and thickness is reduced throughout the simulation years toward average values that are more consistent with satellite observations (Fig. 15a). However, this sea ice coverage reduction is not only a result of the gradual decrease of these parameters around the Southern Ocean but also results from an unrealistic sea ice retreat both in the Weddell Sea and Indian Ocean sectors.





OSD
11, 1023–1091, 2014



Changes in the sea ice concentration directly influence the AABW formation by sea ice melting and brine rejection and also because of their effect on the transference of momentum from wind to ocean currents (Curry and Webster, 1999). In the coupled MITgcm, surface wind stress, as well as heat and fresh water fluxes, are computed from atmospheric states that are modified by a sea ice model at each time step (Adcroft et al., 2012). Therefore, the observed changes in the AABW hydrographic properties from the ECCO2 data can be directly linked to the variations of sea ice concentrations and thickness produced by the model.

The opening of an oceanic polynya is closely related to the process of deep convection occurring in the open ocean regime, which leads to a high production of dense waters that are directly injected in deeper levels (normally below 2000 m) in the open ocean area of the Weddell Sea. Heuze et al. (2013) evaluated 15 climate models and showed that most of them produce dense bottom waters by deep convection in the open ocean, which is closely linked to the representation of a strong sea ice seasonal cycle. A decrease of the sea ice concentration could have enabled a more direct effect of wind stress over the ocean, which could have intensified the Weddell Gyre circulation reproduced by the reanalysis. A stronger gyre intensifies the upwelling of isopycnals at the center of the gyre and leads to warm intermediate waters close to the surface. Consequently, deep convection is increased, and transference of heat to sea ice is enhanced, which leads to the opening of an oceanic polynya. The further retreat of sea ice after the polynya formation also contributes to the intensification of ocean currents and facilitates the spreading of the AABW dense plume. As a result, the hydrographic properties of the Southern Ocean are poorly represented during the most recent years of the ECCO2 reanalysis data.

The dominant variability modes from sea ice, wind stress, and AABW export (relative to *Section* II) are better evaluated through a wavelet analysis (Fig. 16). The sea ice thickness and covered area are averaged within the Weddell Sea sector limits (60° W–20° E) to build monthly time series. The wind stress time series is determined based on a proxy region defined to cover the main area that drives the Weddell Gyre circulation.





OSD
11, 1023–1091, 2014



All series are detrended before the analysis, and only the period 1992–2004 is evaluated. The dominant period of variability of the AABW export is 1 year (Fig. 16c), which is related to the seasonal variation of wind-driven circulation and sea ice formation. The AABW volume transport also reveals a 2–4 year period of variability throughout most of the period evaluated. This pattern is consistent with the 3–4 year oscillation determined by Venegas and Drinkwater et al. (2001) for the coupled sea ice, atmospheric, and oceanic oscillation in the Weddell Sea. The annual cycle is clearly present in the sea ice and meridional wind stress time series (Fig. 16 a, b and f). However, the 2–4 year oscillation is only seen in a short period of the meridional wind stress component.

## 4 Summary and conclusions

An assessment of the ECCO2 data shows that the reanalysis product provides a good quality representation of the main Southern Ocean oceanographic features and the characteristic shape of regional $\theta$–$S$ diagrams. Significant changes can be observed throughout the simulation years, e.g., retreating of the AABW layer in the B&A and Ross Sea sectors. However, the most striking modification observed is the appearance of a dense water plume in the Weddell Sea sector that is related to the opening of an open ocean polynya clearly visible in 2005 at the center of the Weddell Gyre. This phenomenon contributes to the unrealistic representation of the Southern Ocean hydrographic properties primarily after 2004.

The mean difference of the hydrographic properties reproduced by the reanalysis and the observed values in the SL and IL are reduced by approximately 25 % and 21 %, respectively, considering only the reliable period (1992–2004). In general, the ECCO2 reanalysis data show a warmer, saltier, and denser surface layer, whereas intermediate waters are generally colder, fresher, and denser than observations. The exception is the Weddell Sea, which shows slightly warmer and lighter WDW in the center of the Weddell Gyre and WDW outflow region during the reliable period. Those misfits can also be observed in the $\theta$–$S$ diagram by the absence of the cold and fresh surface





OSD
11, 1023–1091, 2014



waters that are seen in the observed values and by the displacement of maximum temperature and salinity of intermediate waters toward lower values. The bottom layer is usually warmer and lighter than expected, which is possibly related to the inability of the reanalysis data to produce the densest AABW variety over a significant portion of the analyzed unfailing period. If the entire period is considered, the average bottom layer is close to observations, which is unrealistic because of the problems indicated toward the end of the ECCO2 simulation.

Comparing the physical properties from repeat hydrographic sections shows that the reanalysis is capable of representing the structure and properties of the main analyzed areas. Specifically considering the sections within the Weddell Sea sector (i.e., WOCE SR2 and WOCE SR4), the AABW upper limit is highly consistent with the area occupied between the reanalysis-observation comparisons. However, the densest AABW regional variety is not represented by the reanalysis for the evaluated sampling periods because it is replaced by the lighter version of the regional AABW varieties. Unlike the other sections, the WOCE SR3 upper dense water limit defined by the different datasets is not well represented. The denser variety of the AABW is also absent in this section, but the limit of this water is deeper than what was expected. The reduced dense layer can also be observed by a comparison of the AABW area estimates for all occupations. This underestimation may be linked to the retraction of dense waters in the B&A and Ross Sea sectors in the ECCO2 simulation.

Several *case studies* show that the structure of deep and bottom current velocity and AABW volume transport are well represented along the sections east of the Antarctic Peninsula (*Section III*), at the Prime Meridian (*Section IV*), and close to the Kerguelen Plateau (*Section I*). The variability pattern of the AABW current velocity and volume transport is consistent with observational data in most cases. The exception is the AABW volume transport determined close to the Kerguelen Plateau. In this region, the low correlation between the reanalysis and observed data may be influenced by a bad representation of the complex local bathymetry, which is further exacerbated by a relatively coarse model resolution. The seasonal cycle is evident in most cases





OSD
11, 1023–1091, 2014



and is mostly induced by wind forcing periodicity. Additionally, a 2–4 year variability period is observed for the AABW export from the Weddell Sea, which is consistent with the coupled sea ice, atmospheric, and oceanic oscillations previously reported in observations (Venegas and Drinkwater, 2001).

Despite the acceptable representation of the AABW volume transport and current velocity variability in the most important region of dense water export, absolute values are underestimated in all cases. The high sea ice concentration during winter months could have limited the transference of momentum from winds to ocean and led to a weaker Weddell Gyre and weaker currents in the ECCO2 reanalysis. A lower wind velocity is also a possible contributing factor, although this characteristic requires further analysis. The relatively coarse model resolution limits the representation of coastal processes and may contribute to the underestimation of dense water export from the shelf regions. Associated with an unrealistic hydrographic representation, the AABW velocity and volume transport are largely enhanced after 2004, leading to values greater than observed.

The ECCO2 is based on the assimilation of a significant amount of observational data throughout the model simulation. Therefore, we expect that in addition to interannual variability, the reanalysis would be capable of representing the observational trends over longer periods. The AABW changing rate determined for the entire Southern Ocean based on the 1992–2004 period shows decreasing cooling, freshening, and density trends. However, these trends are highly influenced by the early cooling of the Weddell Sea and by the reducing contribution of the dense layer in the B&A and Indian sectors, which are the warmest AABW varieties. When the sectors are evaluated separately, warming, freshening, and density decreases are found from 1992 to 2004, excluding the Weddell Sea. The latter warms until 2001, but then undergoes cooling, which may be related to local changes in sea ice concentration and thickness. Both the variability pattern and the changing rate average for all sectors are consistent with trends reported by previously studies that consider all hydrographic properties. The volume decrease of the AABW layer, as shown by the reanalysis data, has also been





OSD
11, 1023–1091, 2014



indicated by observational studies. However, the dramatic retraction of the dense layer in the B&A sector that leads to the absence of waters $\gamma^n \geq 28.27\,\mathrm{kg\,m^{-3}}$ after 2002 has not been observed in the ocean. Moreover, during the unrealistic period (2004–2011), the environmental conditions change and affect the hydrographic property trends.

The results reveal that during the first twelve years (1992–2004) of the simulation, the ECCO2 provides a high quality and reliable representation of hydrographic properties in the Southern Ocean. The differences are related to reanalysis limitations related to the absence of ice shelf representation, model resolution, and parameterizations. These factors also preclude the reanalysis from realistically representing the absolute values of the AABW velocity, volume transport, and outflows from shelf regions. Despite those limitations, the water column structure and the variability of the AABW velocity and volume transport are well represented in the main contributing regions. Another interesting feature presented by the reanalysis is the long-term variability. The reanalysis data are capable of reproducing the long-term variability patterns of observational data reported by previous observations.

Those abilities ensure the use of the 1992–2004 period reanalysis data for AABW circulation and hydrographic studies and for physical process affecting dense water variability. After that period, marked changes of environmental conditions resulting from erroneous sea ice concentrations and thickness cause dramatic changes in the hydrographic properties and distribution as well as in velocity and volume transport. Therefore, the use of data from this latter period (2005–2011) is not advisable. This finding reinforces the need for an accurate representation of sea ice coverage and variability for conducting adequate simulations of Southern Ocean hydrography. Better parameterizations and the inclusion of ice shelves are also factors that must be considered for optimal results. In addition to the limitations of the model and assimilation methodology, reanalysis products can also be biased by problems related to observational data (Dee, 2005). Despite the limitations of the ECCO2 data evaluated in this study, it is important to highlight the improved performance of this reanalysis in reproducing the AABW





OSD
11, 1023–1091, 2014



properties in comparison with other commonly used modeled data, such as OCCAM and ORCA025 (Renner et al., 2009; Kerr et al., 2012).

The ECCO2 is an ongoing project, and several efforts have been made to improve key points, e.g., ice shelf representation. Recent studies have applied regional ECCO2 configurations modified to include explicit representations of ice shelves to investigate the process in the ocean and ice interface (Heimbach et al., 2012; Schodlok et al., 2012; Xu et al., 2012). Moreover, the centerpiece of the ECCO2 is the application of an adjoint-method optimization of the global eddying configuration, which would enable a much larger number of control variables than the Green's function method. The adjoint-method optimization method has already been proven to be valuable (e.g., Mazloff et al., 2010; Ito et al., 2010), and its application both globally and for a longer time period than the actual SOSE (Southern Ocean State Estimation) regional solution would produce a significant improvement.

Finally, long-term observational studies in important regions of the AABW export must be conducted. The focus of these studies should be extended beyond the Weddell and Ross Sea regions to less explored (but also important) areas, such as the Kerguelen Plateau region, which has shown the poorest representation of AABW variability. In addition, the lack of in situ data for winter months affects the quality of reanalysis assimilation and limits the assessment of these datasets and models. The use of new technologies for sampling during wintertime, such as ARGO floats, sea mammals as platforms for data collection, and seagliders, should be encouraged.

**Supplementary material related to this article is available online at http://www.ocean-sci-discuss.net/11/1023/2014/osd-11-1023-2014-supplement.pdf.**

*Acknowledgements.* This study is a contribution to the activities of the Brazilian High Latitudes Oceanography Group (GOAL) in the Brazilian Antarctic Program (PROANTAR). GOAL has been funded by the Brazilian Ministry of the Environment (MMA); the Brazilian Ministry of





OSD
11, 1023–1091, 2014



Science, Technology and Innovation (MCTI); and the Council for Research and Scientific Development of Brazil (CNPq; 550370/2002-1; 520189/2006-0). The authors thank the Brazilian National Institute of Science and Technology of Cryosphere (INCT-CRIOSFERA; 573720/2008-8), the International Polar Year SOS-CLIMATE project, and the POLARCANION project (CNPq 556848/2009-8). MA and RK acknowledge financial support from the CAPES Foundation and FAPERGS. We thank Y. Fukamachi for providing data on the AABW volume transport for the east Kerguelen Plateau. We also acknowledge the Estimating the Circulation and Climate of the Ocean – Phase II (ECCO2) working group for producing and making available their reanalysis output.

## References

Adcroft, A., Dutkiewicz, S., Ferreira, D., Heimbach, P., Jahn, O., and Maze, G.: MITgcm User Manual, 2012.

Aoki, S., Rintoul, S. R., Ushio, S., Watanabe, S., and Bindoff, N. L.: Freshening of the Adélie Land Bottom Water near 140° E, Geophys. Res. Lett., 32, L23601, doi:10.1029/2005GL024246, 2005.

Azaneu, M., Kerr, R., Mata, M. M., and Garcia, C. A. E: Trends in the deep Southern Ocean (1958–2010): implications for Antarctic Bottom Water properties and volume export, J. Geophys. Res., 118, 4213–4227, doi:10.1002/jgrc.20303, 2013.

Boyer, T. P., Antonov, J. I., Baranova, O. K., Garcia, H. E., Johnson, D. R., Locarnini, R. A., Mishonov, A. V., O'Brien, T. D., Seidov, D., Smolyar, I. V., and Zweng, M. M.: World Ocean Database 2009, NOAA Atlas NESDIS, 66, edited by: Levitus, S., DVD, US Gov. Printing Office, Washington, D.C., 2009.

Carmack, E. C. and Foster, T. D.: On the flow of water out of the Weddell Sea, Deep-Sea Res., 22, 711–724, 1975.

Cavalieri, D. J. and Parkinson, C. L.: Antarctic sea ice variability and trends, 1979–2006, J. Geophys. Res., 113, C07004, doi:10.1029/2007JC004564, 2008.

Cavalieri, D. J., Parkinson, C., Gloersen, P., and Zwally, H. J.: Sea ice concentrations from Nimbus-7 SMMR and DMSP SSM/I passive microwave data, January 1979–June 2006, National Snow and Ice Data Center, Boulder, Colorado USA, digital media, 1996, updated 2006, 2006.





OSD
11, 1023–1091, 2014



Condron, A., Winsor, P., Hill, C., and Menemenlis, D.: Simulated response of the Arctic freshwater budget to extreme NAO wind forcing, J. Climate, 22, 2422–2437, 2009.
Curry, J. A. and Webster, P. J.: Sea ice, snow, and glaciers, in: Thermodynamics of Atmospheres and Oceans, 65, chap. 10, edited by: Curry, J. A. and Webster, P. J., 1–471, 1999.
Dee, D. P.: Bias and data assimilation, Q. J. Roy. Meteor. Soc., 131, 3323–3342, 2005.
De la Mare, W. K.: Abrupt mid-twentieth century decline in Antarctic sea ice extent from whaling records, Nature, 389, 57–60, 1997.
Dotto, T. S., Kerr, R., Mata, M. M., Azaneu, M., and Wainer, I.: Assessment of the structure and variability of Weddell Sea water masses in distinct ocean reanalysis products, Ocean Sci. Discuss., 11, 497–542, doi:10.5194/osd-11-497-2014, 2014.
Fahrbach, E., Rohardt, G., Scheele, N., Schroder, N., Strass, V., and Wisotzki, A.: Formation and discharge of deep and bottom water in the northwestern Weddell Sea, J. Mar. Res., 53, 515–538, 1995.
Fahrbach, E., Harms, S., Rohardt, G., Schröder, M., and Woodgate, R. A.: Flow of bottom water in the northwestern Weddell Sea, J. Geophys. Res., 106, 2761–2778, 2001.
Fahrbach, E., Hoppema, M., Rohardt, G., Schröder, M., and Wisotzki, A.: Decadal-scale variations of water mass properties in the deep Weddell Sea, Ocean Dynam., 54, 77–91, 2004.
Fahrbach, E., Hoppema, M., Rohardt, G., Boebel, O., Klatt, O., and Wisotzki, A.: Warming of deep and abyssal water masses along the Greenwich meridian on decadal time scales: the Weddell gyre as a heat buffer, Deep-Sea Res. Pt. II, 58, 2509–2523, 2011.
Foldvik, A., Gammelsröd, T., and Törresen, T.: Circulation and water masses on the southern Weddell Sea shelf, Antarct. Res. Ser., 43, 5–20, 1985.
Foldvik, A., Gammelsrod, T., Osterhus, S., Fahrbach, E., Rohardt, G., Schröder, M., Nicholls, K. W., Padman, L., and Woodgate, R. A.: Ice shelf water overflow and bottom water formation in the southern Weddell Sea, J. Phys. Oceanogr., 109, C02015, doi:10.1029/2003JC002008, 2004.
Foster, T. D. and Carmack, E. C.: Frontal zone mixing and Antarctic Bottom Water formation in the southern Weddell Sea, Deep-Sea Res., 23, 301–317, 1976.
Franco, B., Mata, M. M., Piola, A. R., and Garcia, C. A. E.: Northwestern Weddell Sea deep outflow into the Scotia Sea during the austral summers of 2000 and 2001 estimated by inverse methods, Deep-Sea Res. Pt. I, 54, 1815–1840, 2007.





OSD
11, 1023–1091, 2014



Fukamachi, Y., Rintoul, S. R., Church, J. A., Aoki, S., Sokolov, S., Rosenberg, M. A., and Wakatsuchi, M., Strong export of Antarctic BottomWater east of the Kerguelen plateau, Nat. Geosci., 3, 327–331, 2010.
Gill, A. E.: Circulation and bottom water production in the Weddell Sea, Deep-Sea Res., 20, 111–140, 1973.
Gille, S. T.: Warming of the Southern Ocean since the 1950s, Science, 295, 1275–1277, 2002.
Gordon, A. L.: Deep Antarctic convection west of Maud Rise, J. Phys. Oceanogr., 8, 600–612, 1977.
Gordon, A. L., Huber, B. A., Mckee, D., and Visbeck, M.: A seasonal cycle in the export of bottom water from the Weddell Sea, Nat. Geosci., 3, 551–556, 2010.
Heimbach, P. and Losch, M.: Adjoint sensitivities of sub-ice-shelf melt rates to ocean circulation under the Pine Island Ice Shelf, West Antarctica, Ann. Glaciol., 53, 59–69, 2012.
Hellmer, H. H., Huhn, O., Gomis, D., and Timmermann, R.: On the freshening of the north-western Weddell Sea continental shelf, Ocean Sci., 7, 305–316, doi:10.5194/os-7-305-2011, 2011.
Heuzé, C., Heywood, K. J., Stevens, D. P., and Ridley, J. K.: Southern Ocean bottom water characteristics in CMIP5 models, Geophys. Res. Lett., 40, 1409–1414, 2013.
Huhn, O., Hellmer, H. H., Rhein, M., Rodehacke, C., Roether, W., Schodlok, M. P., and Schröder, M.: Evidence of deep- and bottom-water formation in the western Weddell Sea, Deep-Sea Res. Pt. II, 55, 1098–1116, 2008.
Ito, T., Woloszyn, M., and Mazloff, M.: Anthropogenic carbon dioxide transport in the Southern Ocean driven by Ekman flow, Nature, 463, 80–83, 2010.
Jackett, D. R. and McDougall, T. J.: A neutral density variable for the world's ocean, J. Phys. Oceanogr., 27, 237–263, 1997.
Jacobs, S. S.: On the nature and significance of the Antarctic Slope Front, Mar. Chem., 35, 9–24, 1991.
Jacobs, S. S.: Bottom water production and its links with the thermohaline circulation, Antarct. Sci., 16, 427–437, 2004.
Jacobs, S. S. and Giulivi, C. F.: Large multidecadal salinity trends near the Pacific–Antarctic continental margin, J. Climate, 23, 4508–4524, doi:10.1175/2010JCLI3284.1, 2010.
Jacobs, S. S., Amos, A. F., and Bruchhausen, P. M.: Ross Sea oceanography and Antarctic Bottom Water formation, Deep-Sea Res., 17, 935–962, 1970.





OSD
11, 1023–1091, 2014



Jacobs, S. S., Giulivi, C. F., and Mele, P. A.: Freshening of the Ross Sea during the late 20th century, Science, 297, 386–389, doi:10.1126/science.1069574, 2002.
Johnson, G. C., Purkey, S. G., and Bullister, J. L.: Warming and freshening in the abyssal southeastern Indian Ocean, J. Climate, 21, 5351–5363, 2008.
Kerr, R., Wainer, I., and Mata, M. M.: Representation of the Weddell Sea deep water masses in the ocean component of the NCAR-CCSM model, Antarct. Sci., 21, 301–312, doi:10.1017/S0954102009001825, 2009.
Kerr, R., Heywood, K. J., Mata, M. M., and Garcia, C. A. E.: On the outflow of dense water from the Weddell and Ross Seas in OCCAM model, Ocean Sci., 8, 369–388, doi:10.5194/os-8-369-2012, 2012.
Killworth, P. D.: Deep convection in the world ocean, Rev. Geophys. Space Phys., 21, 1–26, 1983.
Klatt, O., Fahrbach, E., Hoppema, M., and Rohardt, G.: The transport of the Weddell Gyre across the Prime Meridian, Deep-Sea Res. Pt. II, 52, 513–528, 2005.
Lee, T., Awaji, T., Balmaseda, M., Ferry, N., Fujii, Y., Fukumori, I., Giese, B., Heimbach, P., Köhl, A., Masina, S., Remy, E., Rosati, A., Schodlok, M., Stammer, D., and Weaver, A.: Consistency and fidelity of Indonesian-throughflow total volume transport estimated by 14 ocean data assimilation products, Dynam. Atmos. Oceans, 50, 201–223, doi:10.1016/j.dynatmoce.2009.12.004, 2010.
Lumpkin, R. and Speer, K.: Global ocean meridional overturning, J. Phys. Oceanogr., 37, 2550–2562, 2007.
Marshall, J., Adcroft, A., Hill, C., Perelman, L., and Heisey, C.: A finite-volume, incompressible Navier–Stokes model for studies of the ocean on parallel computers, J. Geophys. Res., 102, 5753–5766, 1997.
Maximenko, N. and Niiler, P.: Hybrid decade-mean global sea level with mesoscale resolution, in: Recent Advances in Marine Science and Technology, edited by: Saxena, N., PACON International, Honolulu, 55–59, 2005.
Mazloff, M. R., Heimbach, P., and Wunsch, C.: An eddy-permitting Southern Ocean state estimate, J. Phys. Oceanogr., 40, 880–899, 2010.
McKee, D. C., Yuan, X., Gordon, A. L., Huber, B. A., and Dong, Z.: Climate impact on interannual variability of Weddell Sea Bottom Water, J. Geophys. Res., 116, 1–17, 2011.





OSD
11, 1023–1091, 2014



Meccia, V., Wainer, I., Tonelli, M., and Curchitser, E.: Coupling a thermodynamically active ice shelf to a regional simulation of the Weddell Sea, Geosci. Model Dev., 6, 1209–1219, doi:10.5194/gmd-6-1209-2013, 2013.
Menemenlis, D., Fukumori, I., and Lee, T.: Using Green's functions to calibrate an ocean general circulation model, Mon. Weather Rev., 133, 1224–1240, 2005.
Menemenlis, D., Campin, J. M., Heimbach, P., Hill, C., Lee, T., Schodlok, M., and Zhang, H.: ECCO2: high resolution global ocean and sea ice data synthesis, Mercator Ocean Quarterly Newsletter, 31, 13–21, 2008.
Meredith, M. P., Locarnini, R. A., Van Scoy, K. A., Watson, A. J., Heywood, K. J., and King, B. A.: On the sources of Weddell Gyre Antarctic Bottom Water, J. Geophys. Res., 105, 1093–1104, 2000.
Muench, R. D. and Gordon, A. L.: Circulation and transport of water along the western Weddell Sea margin, J. Geophys. Res., 100, 18503–18515, 1995.
Muench, R. D. and Hellmer, H. H.: The international DOVETAIL program, Deep Sea Res.-Pt. II, 49, 4711–4714, 2002.
Naveira Garabato, A. C., McDonagh, E. L., Stevens, D. P., Heywood, K. J., and Sanders, R. J.: On the export of Antarctic Bottom Water from the Weddell Sea, Deep-Sea Res., 49, 4715–4742, 2002.
Nguyen, A. T., Menemenlis, D., and Kwok, R.: Improved modeling of the Arctic halocline with a subgrid-scale brine rejection parameterization, J. Geophys. Res., 114, C11014, doi:10.1029/2008JC005121, 2009.
Nicholls, K. W., Østerhus, S., Makinson, K., Gammelsrød, T., and Fahrbach, E.: Ice–ocean processes over the continental shelf of the southern Weddell Sea, Antarctica: a review, Rev. Geophys., 47, 1–23, doi:10.1029/2007RG000250, 2009.
Nowlin, W. D., Whitworth III, T., and Pillsbury, R. D.: Structure and transport of the Antarctic Circumpolar Current at Drake Passage from short-term measurements, J. Phys. Oceanogr., 7, 788–802, 1977.
Onogi, K., Tsutsui, J., Koide, H., Sakamoto, M., Kobayashi, S., Hatsushika, H., Matsumoto, T., Yamazaki, N., Kamahori, H., Takahashi, K., Kadokura, S., Wada, K., Kato, K., Oyama, R., Ose, T., Mannoji, N., and Taira, R.: The JRA-25 reanalysis, J. Meteorol. Soc. Jpn., 85, 1–3, 2007.
Orsi, A. H., Nowlin, W. D., and Whitworth, T.: On the circulation and stratification of the Weddell Gyre, Deep-Sea Res. Pt. I, 40, 169–303, 1993.





OSD
11, 1023–1091, 2014



Orsi, A. H., Whitworth III, T., Nowlin Jr., W. D., Whitworth, T., and Nowlin, W. D.: On the meridional extent and fronts of the Antarctic Circumpolar Current, Deep-Sea Res. Pt. I, 42, 641–673, 1995.

Orsi, A. H., Johnson, G. C., and Bullister, J. L.: Circulation, mixing and production of Antarctic Bottom Water, Prog. Oceanogr., 43, 55–109, 1999.

Parkinson, C. L.: Southern Ocean sea ice and its wider linkages: insights revealed from models and observations, Antarct. Sci., 16, 387–400, 2004.

Parkinson, C. L. and Cavalieri, D. J.: Antarctic sea ice variability and trends, 1979–2010, The Cryosphere, 6, 871–880, doi:10.5194/tc-6-871-2012, 2012.

Purkey, S. G. and Johnson, G. C.: Warming of global abyssal and deep Southern Ocean waters between the 1990s and 2000s: contributions to global heat and sea level rise budgets, J. Climate, 23, 6336–6351, 2010.

Purkey, S. G. and Johnson, G. C.: Global contraction of Antarctic Bottom Water between the 1980s and 2000s, J. Climate, 25, 5830–5844, 2012.

Rahmstorf, S.: Thermohaline ocean circulation, in: Encyclopedia of Quaternary Sciences, edited by: Elias, S. A., Elsevier, Amsterdam, 739–750, 2006.

Renner, A. H. H., Heywood, K. J., and Thorpe, S. E.: Validation of three global ocean models in the Weddell Sea, Ocean Model., 30, 1–15, 2009.

Rignot, E., Fenty, I., Menemenlis, D., and Xu, Y.: Spreading of warm ocean waters around Greenland as a possible cause for glacier acceleration, Ann. Glaciol., 53, 257–266, 2012.

Rintoul, S. R.: On the origin and infuence of Adelie Land Bottom Water, in: Ocean, Ice and Atmosphere: Interactions at Antarctic Continental Margin, edited by: Jacobs, S. S. and Weiss, R., Antarctic Research Series, Vol. 75, American Geophysical Union, Washington, D.C., 151–171, 1998.

Rintoul, S. R.: Rapid freshening of Antarctic Bottom Water formed in the Indian and Pacific oceans, Geophys. Res. Lett., 34, 1–5, 2007.

Rintoul, S. R. and Bullister, J. L.: A late winter hydrographic section from Tasmania to Antarctica, Deep-Sea Res. Pt. I, 46, 1417–1454, 1999.

Rintoul, S. R., Sparrow, M., Meredith, M. P., Wadley, V., Speer, K., Hofmann, E., Summerhayes, C., Urban, E., Bellerby, R., Ackley, S., Alverson, K., Ansorge, I., Aoki, S., Azzolini, R., Beal, L., Belbeoch, M., Bergamasco, A., Biuw, M., Boehme, L., Budillon, G., Campos, L., Carlson, D., Cavanagh, R., Charpentier, E., Chul Shin, H., Coffin, M., Constable, A., Costa, D., Cronin, M., De Baar, H., De Broyer, C., De Bruin, T., De Santis, L., Butler, E.,





OSD
11, 1023–1091, 2014



Dexter, P., Drinkwater, M., England, M., Fahrbach, E., Fanta, E., Fedak, M., Finney, K., Fischer, A., Frew, R., Garzoli, S., Gernandt, H., Gladyshev, S., Gomis, D., Gordon, A., Gunn, J., Gutt, J., Haas, C., Hall, J., Heywood, K., Hill, K., Hindell, M., Hood, M., Hoppema, M., Hosie, G., Howard, W., Joiris, C., Kaleschke, L., Kang, S. H., Kennicutt, M., Klepikov, A., Lembke-Jene, L., Lovenduski, N., Lytle, V., Mathieu, P. P., Moltmann, T., Morrow, R., Muelbert, M., Murphy, E., Naganobu, M., Naveira Garabato, A., Nicol, S., O'Farrell, S., Ott, N., Piola, A., Piotrowicz, S., Proctor, R., Qiao, F., Rack, F., Ravindra, R., Ridgway, K., Rignot, E., Ryabinin, V., Sarukhanian, E., Sathyendranath, S., Schlosser, P., Schwarz, J., Smith, G., Smith, S., Southwell, C., Speich, S., Stambach, W., Stammer, D., Stansfield, K., Thiede, J., Thouvenot, E., Tilbrook, B., Wadhams, P., Wainer, I., Willmott Puig, V., Wijffels, S., Woodworth, P., Worby, T., and Wright, S.: The Southern Ocean Observing System: Initial Science and Implementation Strategy, SCAR and SCOR, 74 pp., 2012.

Robertson, R., Visbeck, M., Gordon, A. L., and Fahrbach, E.: Long-term temperature trends in the deep waters of the Weddell Sea, Deep Sea Res.-Pt. II, 49, 4791–4806, 2002.

Roquet, F., Park, Y.-H., Guinet, C., Bailleul, F., and Charrassin, J.-B.: Observations of the Fawn Trough Current over the Kerguelen Plateau from instrumented elephant seals, J. Marine Syst., 78, 377–393, doi:10.1016/j.jmarsys.2008.11.017, 2009.

Schodlok, M., Menemenlis, D., Rignot, E., and Studinger, M.: Sensitivity of the ice shelf ocean system to the sub-ice shelf cavity shape measured by NASA IceBridge in Pine Island Glacier, West Antarctica, Ann. Glaciol., 53, 156–162, 2012.

Schröder, M. and Fahrbach, E.: On the structure and the transport of the eastern Weddell Gyre, Deep Sea Res.-Pt. II, 46, 501–527, 1999.

Schröder, M., Hellmer, H., and Absy, J. M.: On the near bottom variability in the northwestern Weddell Sea, Deep-Sea Res. Pt. II, 49, 4767–4790, doi:10.1016/S0967-0645(02)00158-3, 2002.

Shimada, K., Aoki, S., Ohshima, K. I., and Rintoul, S. R.: Influence of Ross Sea Bottom Water changes on the warming and freshening of the Antarctic Bottom Water in the Australian-Antarctic Basin, Ocean Sci., 8, 419–432, doi:10.5194/os-8-419-2012, 2012.

Talley, L. D.: Closure of the global overturning circulation through the Indian, Pacific, and Southern Oceans: schematics and transports, Oceanography, 26, 80–97, 2013.

Taylor, K. L.: Summarizing multiple aspects of model performance in a single diagram, J. Geophys. Res., 106, 7183–7192, 2001.





OSD
11, 1023–1091, 2014



Van Sebille, E., Spence, P., Mazloff, M. R., England, M. H., Rintoul, S. R., and Saenko, O. A.: Abyssal connections of Antarctic Bottom Water in a Southern Ocean state estimate, Geophys. Res. Lett., 40, 1–6, 2013.

Venegas, S. A. and Drinkwater, M. R.: Sea ice, atmosphere and upper ocean variability in the Weddell Sea, Antarctica, J. Geophys. Res., 106, 16747–16765, 2001.

Volkov, D. L., Fu, L.-L., and Lee, T.: Mechanisms of the meridional heat transport in the Southern Ocean, Ocean Dynam., 60, 791–801, 2010.

Weppernig, R., Schlosser, P., Khatiwala, S., and Fairbanks, R. G.: Isotope data from ice station Weddell: implications for deep water formation in the Weddell Sea, J. Geophys. Res., 101, 25723–25739, 1996.

Whitworth, T., Orsi, A. H., Kim, S. J., Nowlin Jr., W. D., and Locarnini, R. A.: Water masses and mixing near the Antarctic slope front, in: Ocean, Ice, and Atmosphere: Interactions at the Antarctic Continental Margin, edited by: Jacobs, S. S. and Weiss, R. F., Antarctic Research Series, Vol. 75, AGU, Washington, D.C., 1–27, 1998.

Wunsch, C., Heimbach, P., Ponte, R. M., and Fukumori, I.: The global general circulation of the ocean estimated by the ECCO-Consortium, Oceanography, 22, 88–103, 2009.

Xu, Y., Rignot, E., Menemenlis, D., and Koppes, M. N.: Numerical experiments on subaqueous melting of Greenland tidewater glaciers in response to ocean warming and enhanced subglacial discharge, Ann. Glaciol., 53, 229–234, 2012.

Zhang, J., Hibler, W., Steele, M., and Rothrock, D.: Arctic ice–ocean modeling with and without climate restoring, J. Phys. Oceanogr., 28, 191–217, 1998.

Zwally, H. J., Parkinson, C. F., Carsey, P., Gloersen, W. J., Campbell, W. J., and Ramseier, R. O.: Antarctic sea ice variations 1973–75, in: NASA Weather Climate Review, 56, National Aeronautics and Space Administration, Washington, D.C., 335–340, 1979.





OSD
11, 1023–1091, 2014



**Table 1.** Sampling periods from the historical WOCE sections used in the study.

| | Historical WOCE sections | | |
|---|---|---|---|
| | SR4 | SR3 | SR2 |
| Month/year of sampling | Nov 1992<br>Dec 1992–Jan 1993<br>Apr 1996–May 1996<br>Apr 1998<br>Feb 2005–Mar 2005<br>Mar 2008<br>Dec 2010–Jan 2011 | Mar 1993<br>Jan 1994<br>Mar 1996<br>Nov 2001–Dec 2001<br>Jan 2002–Feb 2002<br>Feb 2003–Mar 2003 | Jun 1992<br>Apr 1996<br>Apr 1998–May 1998<br>Mar 1999<br>Dec 2000<br>Dec 2002<br>Feb 2005<br>Feb 2008–Mar 2008<br>Dec 2010 |





OSD
11, 1023–1091, 2014



**Table 2.** Summarized information on the case studies for the velocity and volume transport assessment.

| Case study | Case study I: Kerguelen Plateau/ Indian sector | Case study II: Endurance ridge/ Weddell Sea sector | Case study III: Prime Meridian/ Weddell Sea sector | Case study IV: Western Weddell Sea/ Weddell Sea sector |
|---|---|---|---|---|
| Previous references | Fukamachi et al. (2010) (F10) | Gordon et al. (2010) | Klatt et al. (2005) (K05) and Fahrbach et al. (2011) | Fahrbach et al. (2001) (F01) and Kerr et al. (2012) (K12) |
| Data period | Feb 2003–Jan 2005 | 2000–2007 | 1996–2008 | 1989–1998 |
| Data from previous studies used for comparison | AABW volume transport time series | Current meter time series from moorings M2 and M3 | Zonal velocity from moorings M229 and M233 | WSBW and AABW volume transport time series from F01 and Kerr et al. (2012), respectively; velocity time series from F01 |
| Variables evaluated | AABW volume transport time series | Current velocity time series | Zonal velocity time series | AABW volume transport time series |
| | Averaged velocity field | Neutral density time series | Time series of volume transport for the entire water column and only the AABW layer | WSBW volume transport time series |
| | | | Average cumulative volume transport along the section | |





OSD
11, 1023–1091, 2014



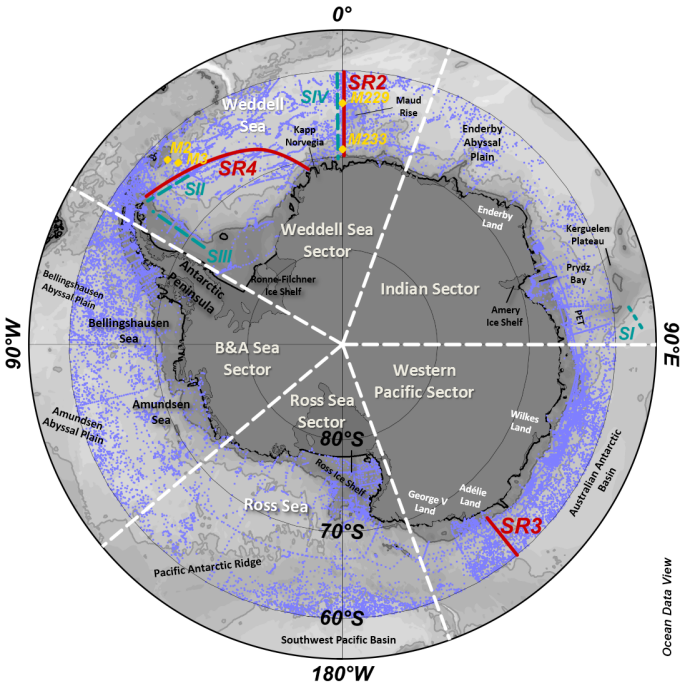


**Fig. 1.** Map indicating the geographic areas of oceanographic profiles (blue dots), hydrographic sections, and mooring positions used in this study. Mooring positions from Klatt et al. (2005) (M233 and M229) and Gordon et al. (2010) (M2 and M3) are indicated by yellow squares. Sections where volume transport was determined (Section I – SI, Section II – SII, Section III – SIII, and Section IV – SIV) are indicated by green dashed lines. Red lines denote the repeat WOCE hydrographic sections used in this study (sampling period are presented in Table 1). Dark and light gray lines refer to the bathymetry of 1300 m and 4000 m, respectively. The radiating white boundary lines delineate hydrographic sectors. B&A denotes the Bellingshausen and Amundsen Sea Sector and PET = Princess Elizabeth Trough.





OSD
11, 1023–1091, 2014



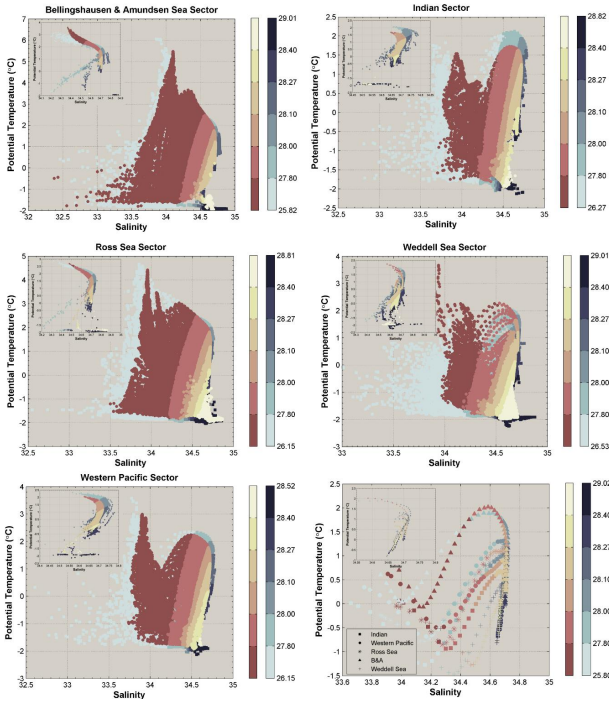


**Fig. 2.** Twenty-year (1992–2011) averaged (summer only) $\theta$–$S$ diagrams for each Southern Ocean sector, as defined in Fig. 1. Inserted panels show $\theta$–$S$ diagrams for the water column deeper than 500 m. The color bars indicate neutral density ($\gamma^n$; kg m$^{-3}$), with the brown (gray) gradient referring to ECCO2 (observations) data. Color bar limits of $\gamma^n = 28.4$ kg m$^{-3}$, $\gamma^n = 28.27$ kg m$^{-3}$, and $\gamma^n = 28.1$ kg m$^{-3}$ were chosen to highlight the points referring to the Weddell Sea Bottom water, Weddell Sea Deep Water, and Warm Deep Water, respectively. The bottom right panel includes the areal average of all Southern Ocean sectors that are distinguished by the marker as indicated by the legend.





OSD
11, 1023–1091, 2014



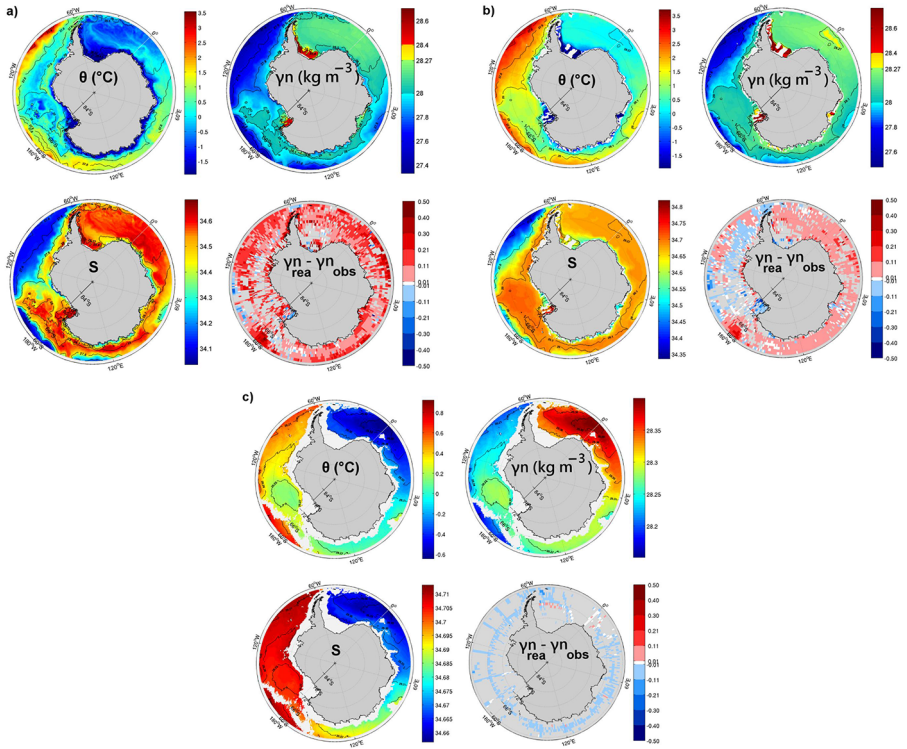


**Fig. 3.** ECCO2 average fields of $\theta$, $S$, and $\gamma^n$ for the **(a)** surface layer – SL (100–150 m), **(b)** intermediate layer – IL (409–634 m), and **(c)** bottom layer – BL (3000 m to seabed). The bottom right panels show the difference between reanalysis and observational density fields.





OSD
11, 1023–1091, 2014



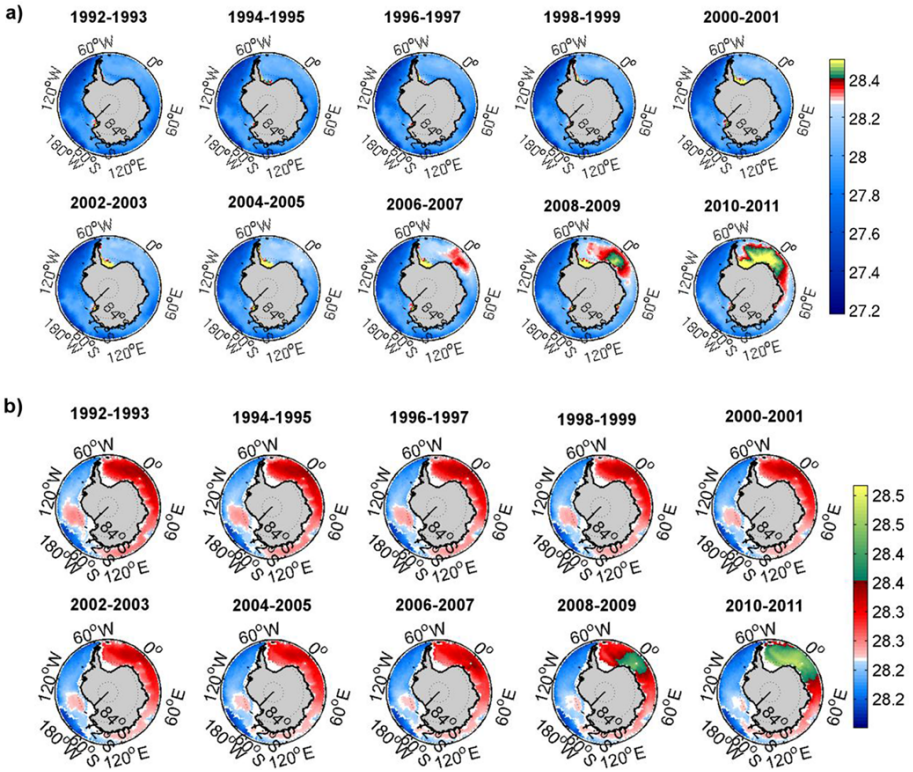


**Fig. 4.** Two-year ECCO2 average density fields of **(a)** surface layer – SL and **(b)** bottom layer – BL. Blue colors denote waters lighter than $\gamma^n = 28.27\,\mathrm{kg\,m^{-3}}$.





OSD
11, 1023–1091, 2014



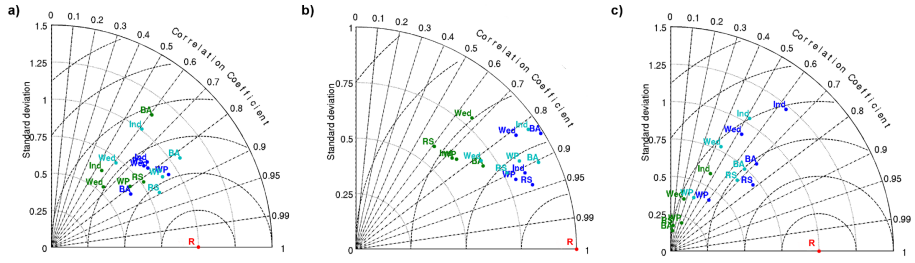


**Fig. 5.** Taylor diagram for each defined layer: **(a)** surface layer – SL (100–150 m), **(b)** intermediate layer – IL (409–634 m), and **(c)** bottom layer – BL (3000 m to seabed) separated by ocean sectors as defined in Figure 1 (Weddell Sea – Wed, Indian – Ind, Western Pacific – WP, Ross Sea – RS, and Bellingshausen and Amundsen Sectors – BA). Dark blue, green, and light blue points indicate $\theta$, $S$, and $\gamma^n$, respectively. The gray curves, black short-dash curves, and black short-dash radii refer to the normalized standard deviation, centered root-mean-square error, and correlation, respectively. R refers to the observed dataset used as reference for comparison (see the text for details).





OSD
11, 1023–1091, 2014



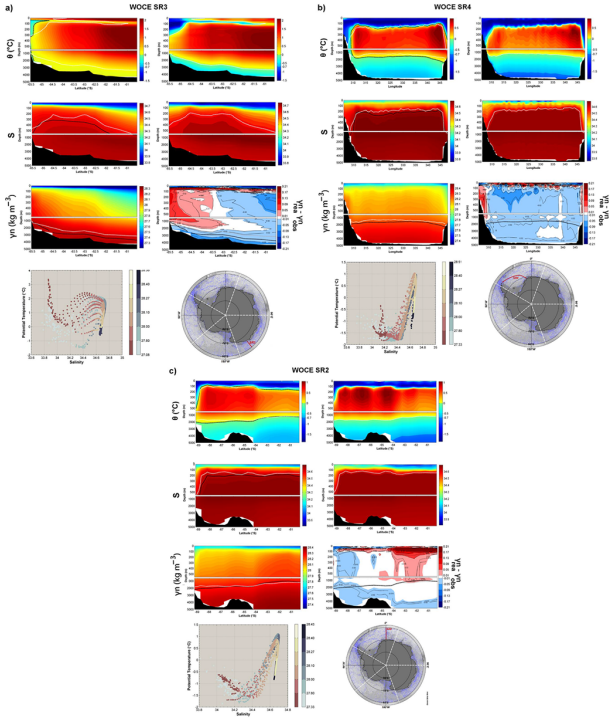


**Fig. 6.** Hydrographic properties of the repeat **(a)** section WOCE SR3, **(b)** section WOCE SR4, and **(c)** section WOCE SR2. Average fields of $\theta$, $S$, and $\gamma^n$ during section occupations for the ECCO2 (left) and observational (right) data. Panels labeled $\gamma^n_{\mathrm{rea}}$–$\gamma^n_{\mathrm{obs}}$ refer to the difference between reanalysis and observational density fields. Dotted lines indicate isolines of $\theta = 0\,^{\circ}\mathrm{C}$, $S = 34.64$, and $\gamma^n = 28.27\,\mathrm{kg\,m^{-3}}$ of the ECCO2 reanalysis (black) and observations (white). The bottom left panels show average $\theta$–$S$ diagrams for the section. The color bar indicates neutral density ($\mathrm{kg\,m^{-3}}$), with a brown (gray) gradient referring to the ECCO2 (observations) data. The bottom right panels show the position of the section on the map.





OSD
11, 1023–1091, 2014



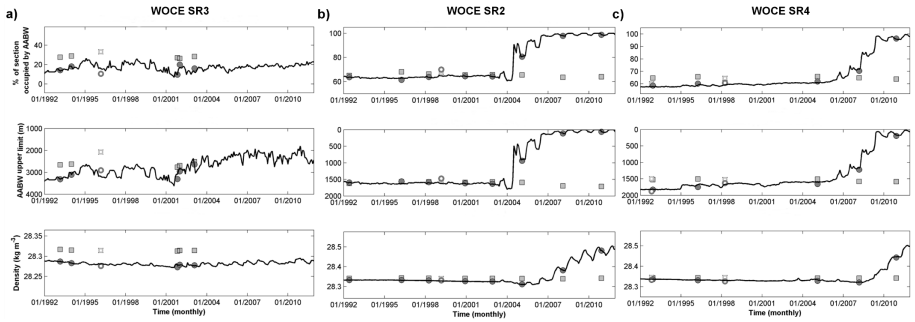


**Fig. 7.** For the WOCE repeat sections, **(a)** SR3, **(b)** SR2, and **(c)** SR4 are presented in the percentage of the section area occupied by the AABW (upper panels), the average upper AABW limit (middle panels), and AABW layer average density (bottom panels). Squares denote observed estimates. Reanalysis estimates limited to in situ data availability are represented by circles. Open markers denote incomplete section occupation. Black lines refer to estimates based on the complete spatial and temporal ECCO2 data.





OSD
11, 1023–1091, 2014



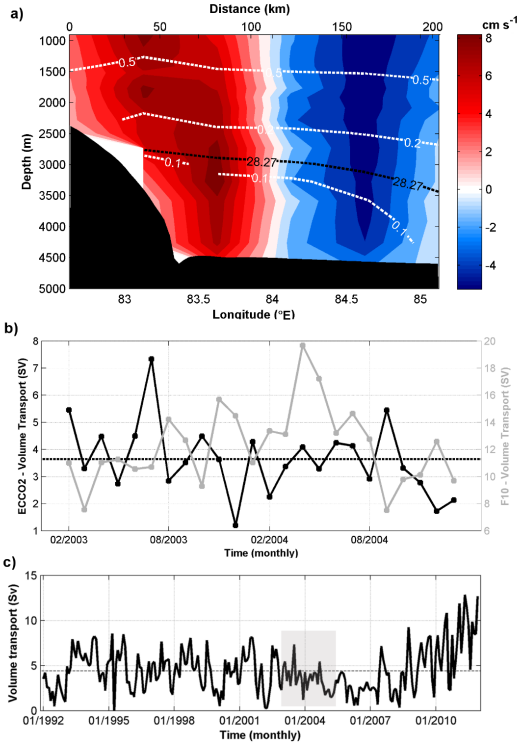


**Fig. 8.** Cross-Section I (see Fig. 1) **(a)** averaged velocity field ($cm\,s^{-1}$) for the period (February 2003–January 2005) evaluated by Fukamachi et al. (2010). White dotted lines indicate isotherms **(b)** Monthly AABW volume transport (Sv) obtained by the ECCO2 data (black line) and Fukamachi et al. (2010) (gray line). The averaged ECCO2 reanalysis estimate is indicated by a black dotted line. **(c)** Monthly AABW volume transport (Sv) for the ECCO2 data during the entire data period. The gray box highlights the period presented in panel **(b)**.





OSD
11, 1023–1091, 2014



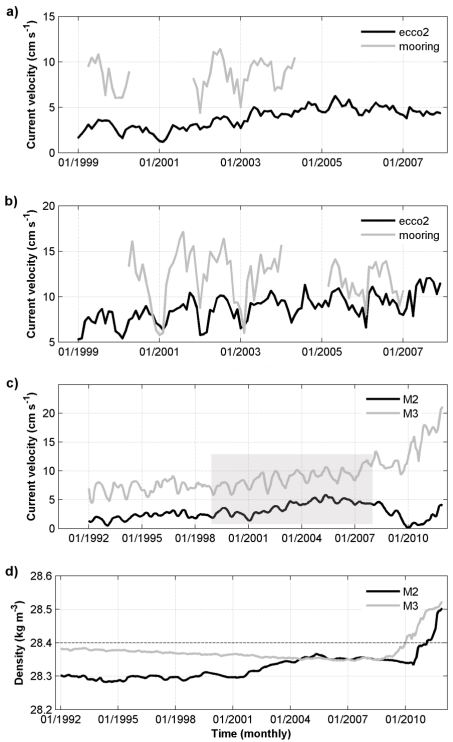


**Fig. 9.** Comparison between monthly time series of current meter (gray) and ECCO2 (black) velocity (cm s$^{-1}$) at **(a)** ~ 4580 m at the M2 position and **(b)** ~ 3100 m at the M3 position (see mooring positions in Fig. 1) and **(c)** monthly ECCO2 time series of current velocity (cm s$^{-1}$) at the M2 position (black line) and M3 position (gray line) from 1992–2011. Both time series are filtered by a three-month window moving average. The boxes highlight periods shown in **(a)** and **(b)**; **(d)** neutral density ($\gamma^n$) of the ECCO2 data at moorings M2 (black) and M3 (gray).





OSD
11, 1023–1091, 2014



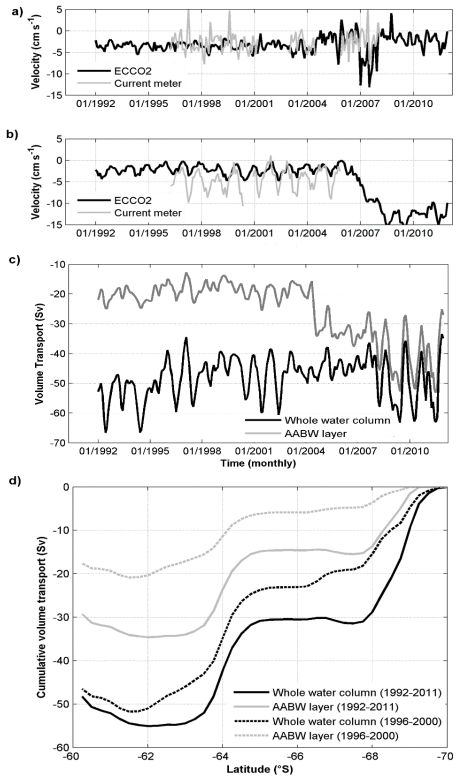


**Fig. 10.** Comparison between monthly time series of current meter (gray) and ECCO2 (black) zonal velocity (cm s$^{-1}$) at ~ 2000 m at the **(a)** M229 and **(b)** M233 positions (see mooring positions in Fig. 1) and **(c)** monthly ECCO2 time series of volume transport (Sv) cross-Section IV considering the entire water column (black line) and only the AABW layer (gray line). Both time series are filtered by a three-month window moving average. **(d)** Cross-Section IV ECCO2 cumulative volume transport for the entire water column (black line) and AABW layer (gray line) for the 1992–2011 period (continuous lines) or limited to the 1996–2000 period (dashed line).





OSD
11, 1023–1091, 2014



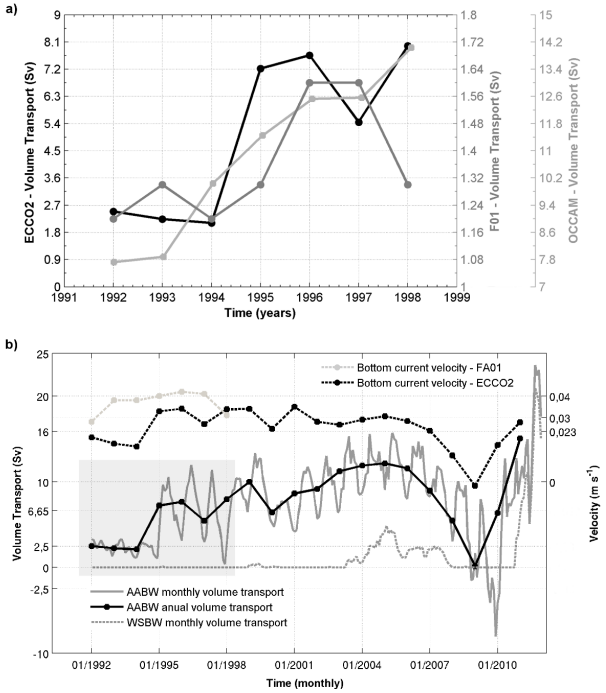


**Fig. 11. (a)** Cross-Section II (Fig. 1) annual transport (Sv) based on the ECCO2 (black line), observational (gray line; from Fahrbach et al., 2001), and OCCAM data (light gray line; from Kerr et al., 2012). The ECCO2 and OCCAM estimates are based on the AABW layer, whereas observational estimates are focused on the WSBW layer. **(b)** The ECCO2 cross-Section II annual (continuous black line) and monthly (continuous gray line) volume transport (Sv) for the AABW layer. Monthly time series considering the WSBW layer are also presented (dashed gray line). The box highlights the estimates presented in **(a)**. Following the right axis, the annual time series velocity from observations (gray line; from Fahrbach et al., 2001) and the ECCO2 data (black line).





OSD
11, 1023–1091, 2014

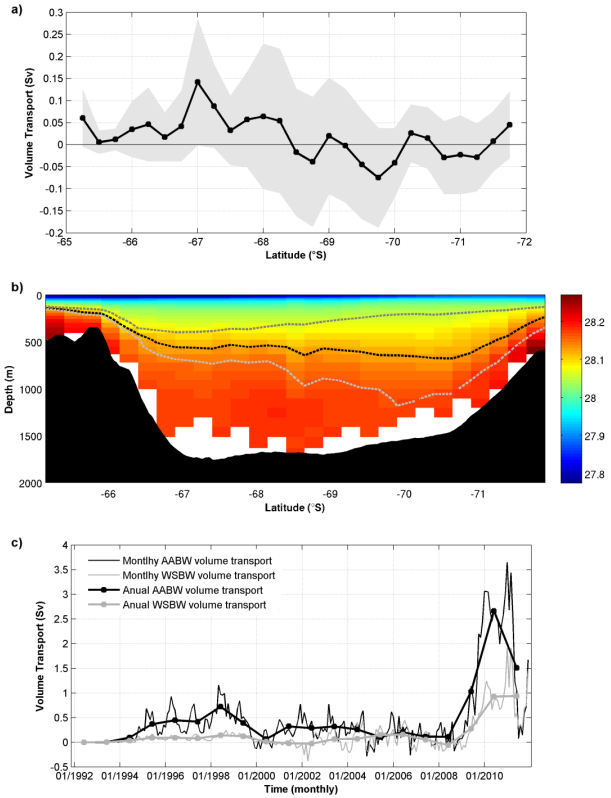


**Fig. 12. (a)** The ECCO2 vertically integrated volume transport cross-Section III of the AABW layer, averaged for 1992–2011 period. Shading indicates the standard deviation of time average. **(b)** Averaged density field along Section II. Black, gray, and light gray dashed lines indicate the AABW average upper limit considering the 1992–2011, 2005–2011, and 1992–2004 periods, respectively. **(c)** Annual (thick lines) and monthly (thin lines) cross section AABW (black lines), and WSBW (gray lines) transport.





OSD
11, 1023–1091, 2014



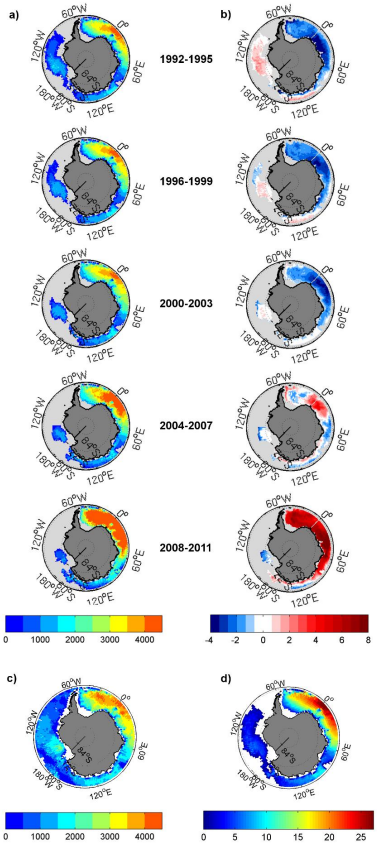


**Fig. 13. (a)** Four-year averages of the AABW layer thickness (m) for the ECCO2 data, 1992–2010. **(b)** The AABW four-year volume anomalies ($m^3$) relative to the long-term (1992–2011) average. **(c)** Twenty-year average AABW layer thickness based on in situ data. **(d)** Twenty-year average AABW layer volume ($10^{12}$ $m^3$) based on reanalysis data.





OSD
11, 1023–1091, 2014



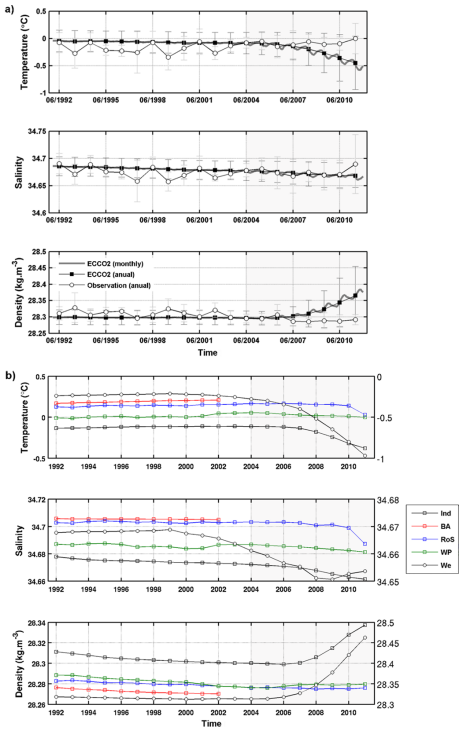


**Fig. 14. (a)** Annual time series of $\theta$, $S$, and $\gamma^n$ for the Southern Ocean AABW layer based on the ECCO2 (filled squares) and observational (open circles) data. The vertical gray bars show the standard deviations of annual averages (reanalysis – dark gray; observations – light gray). **(b)** The ECCO2 annual time series of $\theta$, $S$, and $\gamma^n$ for the Southern Ocean AABW layer for each ocean sector (see Fig. 1): Indian (Ind), B&A (BA), Ross Sea (RoS), Western Pacific (WP), and Weddell Sea (We). The latter follows the right axis of the discrepant values. Shaded regions indicate the period during which the reanalysis reproduced unrealistic hydrographic conditions in the Southern Ocean.





OSD
11, 1023–1091, 2014



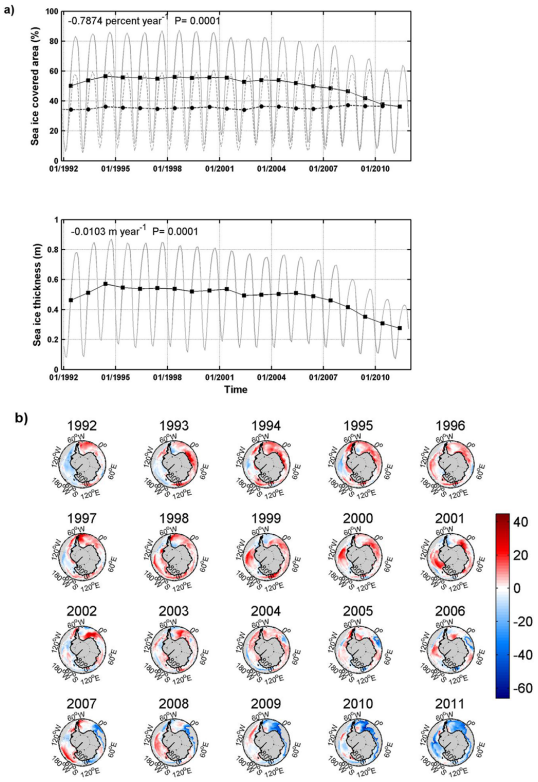


**Fig. 15. (a)** The upper panel shows a comparison of monthly (gray) and annual (black) time series of sea ice-covered area (%) from the ECCO2 (continuous line) and remote sensing (dashed line) data. The bottom panel shows monthly (gray) and annual (black) time series of sea ice thickness from the ECCO2 data. **(b)** ECCO2 sea ice-covered area (%) annual anomalies relative to the long-term (1992–2011) average.





OSD
11, 1023–1091, 2014



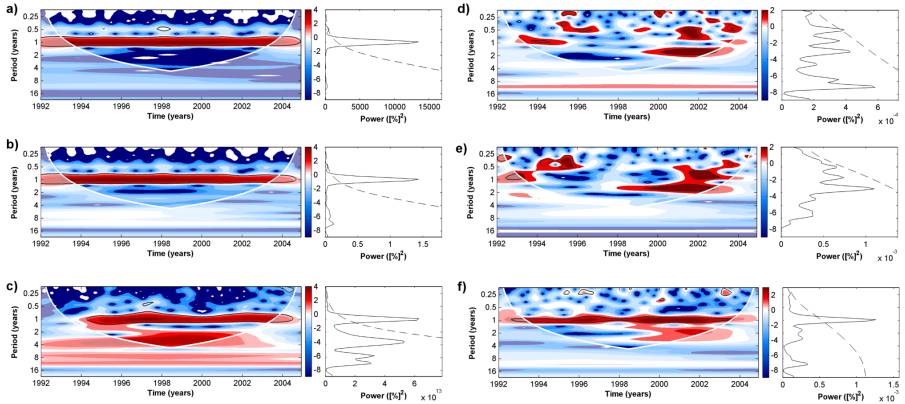


**Fig. 16.** Wavelet power spectrum of **(a)** sea ice-covered area, **(b)** sea ice thickness, **(c)** AABW export in Section II, **(d)** wind stress, **(e)** zonal wind stress, and **(f)** meridional wind stress time series using the Morlet wavelet. The shaded area is the cone of influence, where zero padding has reduced the variance. The black contour encloses regions where confidence levels were greater than 95 %. Energy units (color bar) are in $\log_2$ form. The left panels show the average energy spectrum. The dashed line indicates the 95 % confidence level.





OSD
11, 1023–1091, 2014